AD-A155 529 ALGEBRAIC GRID GENERATION ABOUT A FIN-AFTERBODY CONFIGURATION(U) PENNSYLVANIA STATE UNIV UNIVERSITY PARK APPLIED RESEARCH LAB G H HOFFMAN 12 APR 85 1/1

UNCLASSIFIED ARL/PSU/TM-85-57 N00024-79-C-6043 F/G 12/1 NL

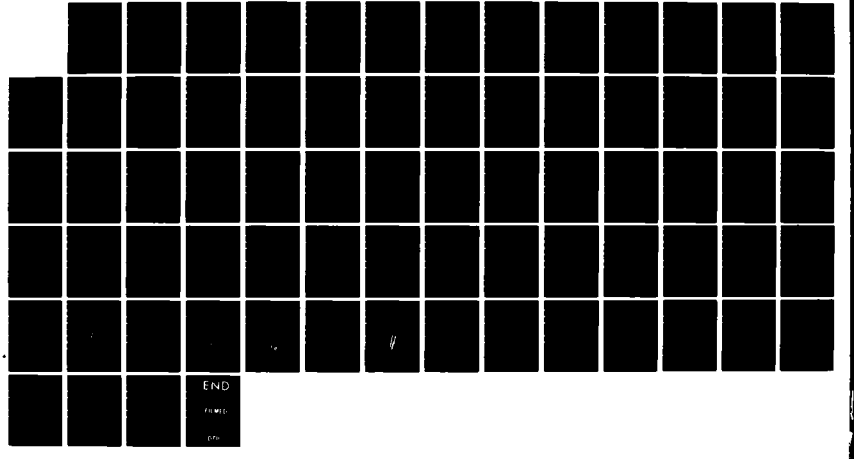

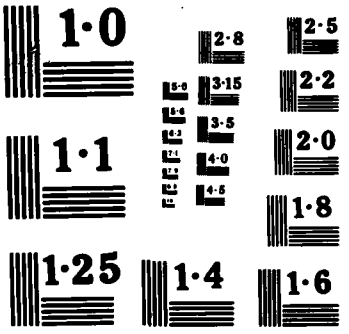

NATIONAL BUREAU OF STANDARDS
MICROCOPY RESOLUTION TEST CHART

(2)

: ARL/PSU TM 85-57

Gilbert H. Hoffman

12 April 1985

1

Correction

r. Thomas E. Peirce, NSEA 63R-31
r. William C. Sandberg, NSEA 55W33

the auspices of the Accelerated Rese
on Hull Propulsor Interaction.

The Pennsylvania State University
Intercollege Research Programs and Facilities
APPLIED RESEARCH LABORATORY
Post Office Box 30
State College, Pa. 16801

NAVY DEPARTMENT

NAVAL SEA SYSTEMS COMMAND

Erratum

Title: Algebraic Grid Generation about a Fin-Afterbody Configuration.

Report No.: ARL/PSU TM 85-57

Author: Gilbert H. Hoffman

Date: 12 April 1985

Page: 1

Correction

Acknowledgment:

This work was sponsored jointly by

Dr. Choung M. Lee, ONR Code 432
Dr. Thomas E. Peirce, NSEA 63R-31
Mr. William C. Sandberg, NSEA 55W33

under the auspices of the Accelerated Research Option on Hull Propulsor Interaction.

ALGEBRAIC GRID GENERATION ABOUT A FIN-AFTERBODY CONFIGURATION

G. H. Hoffman

Technical Memorandum
File No. TM 85-57
12 April 1985
Contract N00024-79-C-6043

Copy No. 1

The Pennsylvania State University
Intercollege Research Programs and Facilities
APPLIED RESEARCH LABORATORY
Post Office Box 30
State College, PA 16804

NAVY DEPARTMENT

NAVAL SEA SYSTEMS COMMAND

UNCLASSIFIED

SECURITY CLASSIFICATION OF THIS PAGE (When Data Entered)

REPORT DOCUMENTATION PAGE		READ INSTRUCTIONS BEFORE COMPLETING FORM
1. REPORT NUMBER TM 85-57	2. GOVT ACCESSION NO.	3. RECIPIENT'S CATALOG NUMBER
4. TITLE (and Subtitle) ALGEBRAIC GRID GENERATION ABOUT A FIN-AFTERBODY CONFIGURATION		5. TYPE OF REPORT & PERIOD COVERED Technical Memorandum 6. PERFORMING ORG. REPORT NUMBER
7. AUTHOR(s) Gilbert H. Hoffman		8. CONTRACT OR GRANT NUMBER(s) N00024-79-C-6043
9. PERFORMING ORGANIZATION NAME AND ADDRESS Applied Research Laboratory Post Office Box 30 State College, PA 16804		10. PROGRAM ELEMENT, PROJECT, TASK AREA & WORK UNIT NUMBERS
11. CONTROLLING OFFICE NAME AND ADDRESS Naval Sea Systems Command, Code NSEA-05R24 Department of the Navy Washington, DC 20362		12. REPORT DATE 12 April 1985 13. NUMBER OF PAGES 69
14. MONITORING AGENCY NAME & ADDRESS (if different from Controlling Office)		15. SECURITY CLASS. (of this report) UNCLASSIFIED 15a. DECLASSIFICATION DOWNGRADING SCHEDULE

16. DISTRIBUTION STATEMENT (of this Report)

Approved for public release. Distribution unlimited.
Per NAVSEA -- 20 May 1985

17. DISTRIBUTION STATEMENT (of the abstract entered in Block 20, if different from Report)

18. SUPPLEMENTARY NOTES

19. KEY WORDS (Continue on reverse side if necessary and identify by block number)

grid generation
afterbodies with fins

20. ABSTRACT (Continue on reverse side if necessary and identify by block number)

An algebraic procedure is presented for the generation of a smooth computational grid about an afterbody-fin configuration. The method makes use of a sequence of conformal transformations to unwrap the geometry and remove the corner singularities at the fin trailing edge and tail of the afterbody. A 3-D grid is generated by stacking a sequence of 2-D grids of the C-type on predetermined, smooth tubular

DD FORM 1 JAN 73 1473 EDITION OF 1 NOV 65 IS OBSOLETE

UNCLASSIFIED

SECURITY CLASSIFICATION OF THIS PAGE (When Data Entered)

surfaces. Clustering is accomplished by a sequence of one-dimensional stretching functions in physical space. Examples are presented to show the character of the resulting grid.

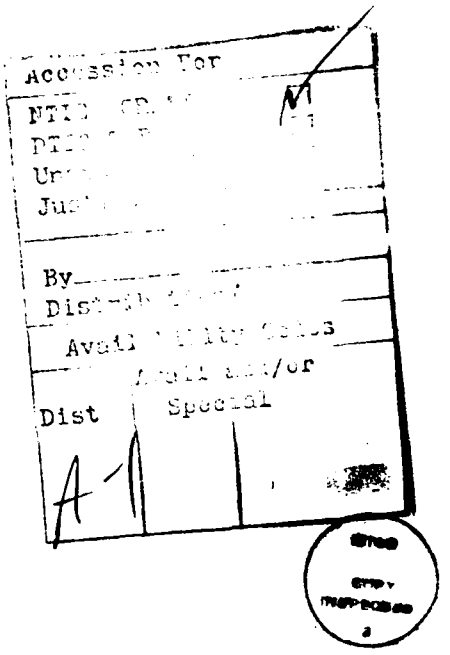

From: G. H. Hoffman

Subject: Algebraic Grid Generation about a Fin-Afterbody Configuration

Abstract: An algebraic procedure is presented for the generation of a smooth computational grid about an afterbody-fin configuration. The method makes use of a sequence of conformal transformations to unwrap the geometry and remove the corner singularities at the fin trailing edge and tail of the afterbody. A 3-D grid is generated by stacking a sequence of 2-D grids of the C-type on predetermined, smooth tubular surfaces. Clustering is accomplished by a sequence of one-dimensional stretching functions in physical space. Examples are presented to show the character of the resulting grid. The computer code, which also contains a user's manual, is available from the author.

Acknowledgment: This work was supported by Naval Sea Systems Command, Code NSEA 05R24.

TABLE OF CONTENTS

	Page
Abstract	1
Acknowledgment	1
Nomenclature	3
List of Figures	4
List of Tables	5
1. Introduction	6
2. Analysis	9
2.1 Geometry of Computational Domain	9
2.2 Grid Stacking Procedure	10
2.3 Grid Generation on a Tubular Surface	16
Overall Approach	16
Sequence of Transformations	16
Corner Point Projection on Airfoil	19
Stretching Functions	20
Transfinite Interpolation	22
Addon Grid	24
2.4 Computational Grid	24
3. Results and Discussion	26
References	32
Figures	33
Appendix I. Conformal Mapping Relations	57
Appendix II. Evaluation of Boundary Derivatives for Transfinite Interpolation	60

NOMENCLATURE

d_{BOD}	length of afterbody
d_{IVL}	distance from leading edge of airfoil to initial value line
d_{OB}	distance from tail of body to outflow boundary
d_{TL}	distance from trailing edge of airfoil to tail of afterbody
JMAX	number of grid points on stagnation line
KMAX	number of stacked surfaces, radial direction
N1	number of grid intervals on airfoil between leading edge and point K
N2	number of grid intervals on airfoil between point K and trailing edge
N3	number of grid intervals on afterbody between airfoil trailing edge and end of body
N4	number of grid intervals between tail of body and outflow boundary
SX0	grid clustering parameter at airfoil leading edge
SX1	grid clustering parameter at point K on Segment 1
SX2	grid clustering parameter at airfoil trailing edge
SX3	grid clustering parameter at tail of body
SY0	grid clustering parameter on stagnation line at airfoil leading edge
SY1	grid clustering parameter on stagnation line at initial value surface
SZ0	grid clustering parameter on afterbody surface in radial direction

All other symbols are defined in the text.

LIST OF FIGURES

		Page
Figure 1.	Schematic of Geometry and Computational Domain	33
Figure 2.	Planes of Symmetry	34
Figure 3.	Grid in Meridian Plane using Shearing Transformation	35
Figure 4.	Meridian Plane View of Geometry and Computational Domain	36
Figure 5.	Meridian Boundary Image in Hinge Plane	37
Figure 6.	Computational Domain, $\bar{r}$ = Constant Surface	38
Figure 7.	Boundaries in $\xi - \eta$ Plane	39
Figure 8.	Boundaries in Positive $\bar{\xi} - \bar{\eta}$ Plane	40
Figure 9.	Translated and Rotated Boundaries in $\hat{x} - \hat{y}$ Plane	41
Figure 10.	Boundaries in Hinge Plane	42
Figure 11.	Typical Grid in Hinge Plane using Transfinite Interpolation	43
Figure 12.	Case 1, No Clustering at Point K	44
Figure 13.	Case 2, Clustering at Point K	45
Figure 14.	Case 3, Clustering at Airfoil Surface	46
Figure 15.	Case 4, Intermediate Upstream Position of Initial Value Line	47
Figure 16.	Case 5, Extreme Upstream Position of Initial Value Line	48
Figure 17.	Meridian Plane View of Test Problem Geometry	49
Figure 18.	Front View of Afterbody Grid	50
Figure 19.	Side View of Afterbody Grid	51
Figure 20.	Front View of Intermediate Surface Grid	52
Figure 21.	Side View of Intermediate Surface Grid	53
Figure 22.	Front View of Outer Surface Grid	54
Figure 23.	Side View of Outer Surface Grid	55
Figure 24.	Composite View of Afterbody, Intermediate and Outer Surface Grids	56

LIST OF TABLES

Page

Table 1. Common Parameters in 2-D Test Cases 27

Table 2. Variable Parameters in 2-D Test Cases 27

Table 3. Parameters in 3-D Test Problem 29

1. Introduction

Algebraic grid generation methods for three-dimensional (3-D) flow problems have the advantage over their differential equation counterparts in speed and ability to handle high aspect ratio cells without difficulty. Where the algebraic methods are sometimes at a disadvantage is in treating a wide variety of boundary shapes with a single code.

Since 1979 grids about wing-body configurations have been successfully generated by several algebraic approaches. Eriksson [1] has generated a single-block nonorthogonal 3-D grid using transfinite interpolation where geometric data is specified only on the boundaries. Since no internal surfaces are specified, grid quality is controlled, especially near a surface, by incorporating out-of-surface parametric derivatives. Smith [2] uses the patched grid approach where the domain is divided into regions with boundaries of a simpler character than the overall region. On the interior of each six-sided sub-region transfinite interpolation is used to generate the grid. His treatment extends only to the wing tips which limits its usefulness. A third and quite different approach has been taken by Caughey & Jameson [3]. Their technique generates a boundary-conforming coordinate system by a sequence of conformal and shearing transformations to yield a nearly orthogonal computational domain. The grid is then generated by simple linear interpolation. Shmilovich & Caughey [4] have recently extended this technique to include a tail surface. The Caughey-Jameson procedure was developed for use with the 3-D transonic FLO codes.

One of the major difficulties in algebraic grid generation is preventing corner singularities on the boundaries from propagating into the grid. Any interpolation method will propagate such singularities into the interior.

Differential equation grid generation schemes suffer no such problem because of the diffusive action of the elliptic operator. Corner singularities are always present in 3-D configurations at wing/fin trailing edges and tail points on pointed bodies. A method for removing these singularities in algebraic grid generation has been developed by Vinokur & Lombard [5] for 2-D geometries. Their method consists of patching a conformal hinge point transformation in a small region near the corner to a grid in the remainder of the domain generated by transfinite interpolation. They successfully applied this method in generating a patched grid in a domain consisting of a backward facing step at the end of a nozzle exhausting into a cylindrical diffuser.

The problem treated in this report is the generation of a surface fitted grid in the stern region of an undersea vehicle, specifically an axisymmetric pointed afterbody with four identical, symmetric, constant chord fins. In many respects this problem is similar to the wing-fuselage problem. The desired grid is to be used for either inviscid or viscid incompressible flow calculations and hence must have proper clustering ability to resolve regions of high flow gradients. An algebraic approach is used which is an outgrowth of earlier 3-D grid generation work on a fin-cylinder configuration [6].

The algebraic method adopted here was originally inspired by the work of Caughey & Jameson in unwrapping a geometry as much as possible to produce a parallelpiped with nearly straight boundaries. This procedure is of the stacking type where a 3-D grid is produced by a sequence of 2-D grid generation operations. In the present method stacked tubular surfaces of circular cross-section are first determined and then a C-type grid generated

on each surface. In the process of generating these surfaces as well as in unwrapping the airfoil, corner singularities are removed by application of a hinge point transformation to the entire boundary. The present approach thus differs from that of Vinokur & Lombard in being global rather than local in the use of the hinge point transformation. The result is a smooth boundary with a slowly varying tangent. A grid which is orthogonal at all boundaries is then generated on the interior by transfinite interpolation. By using a sequence of one-dimensional stretching functions in physical space, precise control is maintained over the clustering at all boundaries.

2. Analysis

2.1 Geometry of Computational Domain

We start by defining the geometry for which a surface-fitted grid is to be generated.

(1) The afterbody is of circular cross-section and has a smooth but otherwise arbitrary meridian profile that closes at the tail point.

(2) Four identical fins of constant unit chord and infinite span, consisting of symmetric airfoil sections, are mounted 90 degrees apart with their chord planes passing through the afterbody centerline. The trailing edges of the fins are located upstream of the tail point a distance d_{TL}.

(3) The computational domain consists of the region interior to an outer cylinder of radius r_{TIP} and exterior to the afterbody, bounded upstream and downstream by planes normal to the afterbody centerline (the initial value and outflow planes).

A schematic of the geometry and computational domain is shown in Fig. 1 and a head-on view showing the coordinate system in the crossflow plane appears in Fig. 2. Since the fins are identical and equally spaced there are four planes of symmetry at $\theta = 0$, $\pi/4$, $\pi/2$ and $3\pi/4$. Thus, only the section $-\pi/4 \leq \theta \leq 0$ is considered in generating a grid and in the flowfield calculation.

2.2 Grid Stacking Procedure

The simplest grid stacking scheme, such as that in Ref. 3, makes use of a shearing transformation to distribute a sequence of two-dimensionally produced grids in the third spatial direction. Unfortunately the shearing transformation causes surface corner discontinuities to propagate into the grid. In the present case of a pointed tail body, Fig. 3 illustrates the situation that would exist in the meridian plane if a shearing transformation were used. Along the vertical line through the tail point, $x = x_T$, lines of constant η have discontinuous slopes.

What is needed is a transformation to produce η = constant lines that does not propagate corner discontinuities. The hinge point (power law) conformal transformation has this desired property. At the tail point (corner discontinuity) we write

$$w = z^n \quad , \tag{1}$$

where the real axis is aligned with the axis of symmetry, and

$$z = x + iy \quad , \tag{2}$$

$$w = u + iv \quad , \tag{3}$$

$$n = \frac{\pi}{\pi - \hat{\theta}_T} \quad . \tag{4}$$

The tail angle $\hat{\theta}_T$ is defined in the meridian plane schematic given in Fig. 4. Equation (1) maps the sector $0 \leq \hat{\theta} \leq \pi - \hat{\theta}_T$ above the real axis onto the upper half plane. If Eq. (1) is applied to the entire bounding curve in the meridian plane, A-B-C-D-E-A, the corner at the tail point B is

eliminated in the w (hinge) plane. Then interpolating a grid in the hinge plane, upon transformation, will produce a smooth grid (except at B) in the physical plane which can be used for stacking.

Before proceeding further, we present the calculational steps in going from the z plane to the w plane and vice-versa. We start by writing z and w in polar form,

$$z = \hat{r}e^{i\hat{\theta}} \quad , \quad w = \rho e^{i\phi} \quad . \tag{5}$$

Then substituting Eqs. (5) into Eq. (1) and equating real and imaginary parts gives

$$\left.\begin{aligned} \rho &= \hat{r}^n \\ \phi &= n\hat{\theta} \end{aligned}\right\} \quad . \tag{6}$$

Given (x,y), to compute (u,v) we first compute the magnitude $\hat{r}$ and angle $\hat{\theta}$ from

$$\left.\begin{aligned} \hat{r} &= \left(x^2 + y^2\right)^{1/2} \quad , \\ \hat{\theta} &= \begin{cases} \tan^{-1}\left(\frac{y}{x}\right) + \pi & , \quad x < 0 \\ \frac{\pi}{2} & , \quad x = 0 \\ \tan^{-1}\left(\frac{y}{x}\right) & , \quad x > 0 \end{cases} \end{aligned}\right\} \quad . \tag{7}$$

Next, ρ and ϕ are computed from Eq. (6) and finally u and v (transforming from polar to cartesian form) from

$$\left.\begin{aligned} u &= \rho \cos \phi \quad , \\ v &= \rho \sin \phi \quad . \end{aligned}\right\} \quad . \tag{8}$$

Conversely, if (u,v) are given, the magnitude ρ and angle ϕ are computed from

$$\left.\begin{aligned} \rho &= \left(u^2 + v^2\right)^{1/2} \quad , \\ \phi &= \begin{cases} \tan^{-1}\left(\frac{v}{u}\right) + \pi & , \quad u < 0 \\ \frac{\pi}{2} & , \quad u = 0 \\ \tan^{-1}\left(\frac{v}{u}\right) & , \quad u > 0 \end{cases} \end{aligned}\right\} \quad . \tag{9}$$

Then $\hat{r}$ and $\hat{\theta}$ are computed from the inverse of Eq. (6), viz.

$$\left.\begin{aligned} \hat{r} &= \rho^{1/n} \\ \hat{\theta} &= \frac{1}{n}\,\phi \end{aligned}\right\} \quad . \tag{10}$$

Finally, x and y are related to $\hat{r}$ and $\hat{\theta}$ by

$$\left.\begin{aligned} x &= \hat{r} \cos \hat{\theta} \\ y &= \hat{r} \sin \hat{\theta} \end{aligned}\right\} \quad . \tag{11}$$

The image of boundary A-B-C-D-E-A in the hinge plane is shown schematically in Fig. 5 and has the appearance of a water spout. Segment BC remains straight because the real axis in the z plane is coincident with

BC. For convenience, the transformed boundary segments will be denoted by point-of-compass notation. Thus A-B-C is $v_S(u)$ and E-D is $v_N(u)$.

To accommodate the inflow and outflow boundaries (lines A-E and C-D in Fig. 5) as well as the leading and trailing edges of the fin, vertical lines must remain vertical in the physical plane. This requirement acts as a constraint on the transformation from the hinge to the physical plane.

The simplest scheme for producing a grid in the hinge plane is a shearing transformation on the image of x = constant lines. Thus the normalized variable $\bar{r}$ is defined as

$$\bar{r} = \left(\frac{v - v_S}{v_N - v_S}\right)_{x=\text{const.}} \quad . \tag{12}$$

At this point the distribution of $\bar{r}_j$ is assumed known. Thus in the interior v is given by

$$v_{i,j} = v_{S_i} + \bar{r}_j \left(v_N - v_S\right)_i \quad , \tag{13}$$

where the index i is constant on x = constant lines.

Thus at point (i,j) the values of x_i and $v_{i,j}$ are known. Then $(y,u)_{i,j}$ are determined by iteratively solving Eq. (1) as follows: A first guess for y is obtained by linear interpolation from

$$y^{(1)}_{i,j} = y_{S_i} + \bar{r}_j \left(y_N - y_S\right)_i \quad . \tag{14}$$

The cycle begins by computing u from

$$u = \hat{r}^n \cos\left(n\hat{\theta}\right) \quad , \tag{15}$$

where $\hat{r}$ and $\hat{\theta}$ are given by Eqs. (7). Next, new values of ρ and ϕ, corresponding to the current estimate of u and the known v, are computed from Eqs. (9). The ρ and ϕ are then used to update $\hat{r}$ and $\hat{\theta}$ using Eqs. (10), and finally, x_c and y are given by Eqs. (11). Convergence is attained when

$$|x - x_c| < 10^{-6} \quad . \tag{16}$$

Thus for each value of $\bar{r}$ = constant, a smooth curve $y_s(x)$ is determined in the meridian plane using the above procedure. By revolving $y_s(x)$ about the x-axis a tubular coordinate surface is obtained which is smooth and non-developable (except when it is a cylinder). On each of these surfaces a surface fitted grid is determined as though the surface were developable, then projected back onto the surface. This means that given (x,θ), r is determined by interpolation of the tubular meridian-plane curve $r_s(x) = y_s(x)$. For the projection method to work properly, the foil subtended angle $\theta_F(x)$ must be computed to account for the variable $r_s(x)$ from

$$\theta_F = \sin^{-1}\left(\frac{y_F}{r_s}\right) \tag{17}$$

where $y_F(x)$ is the airfoil semi-thickness distribution. Lagrange cubic interpolation is used to determine r, given x, from the previously determined values of r_s.

Clustering of $\bar{r}$ = constant lines near the body surface is needed to resolve the viscous layer whereas further away, where flow gradients diminish, these lines can be further apart. A one-sided stretching function is therefore appropriate to determine the grid line spacing in the meridian plane.

Vinokur [7] has determined approximate criteria for the development of one- and two-sided stretching functions of one variable which give a uniform truncation error independent of the governing differential equation or difference algorithm. He investigates several analytic functions but finds that only tan z, where z is real or pure imaginary, satisfies all of his criteria. These stretching functions were used in the predecessor grid generation scheme [6] and are also used here.

Since $\bar{r}$ is already a normalized variable, its distribution is given by

$$\bar{r} = 1 + \frac{\tanh\left[\frac{1}{2}\,\Delta\phi\left(\xi - 1\right)\right]}{\tanh\frac{\Delta\phi}{2}} \quad , \tag{18}$$

where ξ is the normalized generating variable given by

$$\xi = \frac{j - 1}{N_{\bar{r}}} \quad ,$$

and $\Delta\phi$ is the solution of

$$S_0 = \frac{\sinh\,\Delta\phi}{\Delta\phi} \quad , \tag{19}$$

and

$$S_0 = \frac{d\xi}{d\bar{r}}\,(0) \quad ,$$

$N_{\bar{r}}$ = number of intervals in $\bar{r}$ = KMAX - 1 .

2.3 Grid Generation on a Tubular Surface

Overall Approach

Grid generation in the x - θ plane is accomplished in three stages. The first stage involves a sequence of conformal transformations to unwrap the airfoil, symmetry lines and initial and outflow lines into a quadrilateral with a slowly varying height. The unwrapping transformations are the basis for producing a C-grid about the airfoil. The second stage involves translation and rotation of coordinates about the image of the airfoil trailing edge, followed by a hinge point transformation to eliminate the corner at the trailing edge. The third stage makes use of transfinite interpolation to determine the grid in the hinge plane that is orthogonal at all boundaries. Since the boundaries in the hinge plane are smooth and have a slowly varying tangent, transfinite interpolation will produce a smooth grid in which non-orthogonality in the interior is held to a minimum. The grid in the physical plane is obtained by taking the inverse of the sequence of transformations. Since the intermediate transformations are conformal, the orthogonality at boundaries and grid smoothness will be preserved in the physical plane. Spacing of grid lines is determined on appropriate boundaries in the physical plane by use of stretching functions.

Sequence of Transformations

At this stage the coordinates of the fin (x_F, ϑ_F) on a specified $\bar{r}$ = constant tubular surface are assumed known. The first step, in preparation for the unwrapping transformation, is to scale the (x,θ) coordinates according to

$$\left.\begin{aligned} \bar{x} &= 4(x - d_s) + \ell n\ 2 \\ \bar{\theta} &= 4\theta \end{aligned}\right\} \qquad (20)$$

where d_s is the location of the singular point in the unwrapping transformation and is just inside the leading edge of the airfoil. The stretching factor 4 is required by the unwrapping transformation so that the upper limit on $\bar{\theta}$ will be $\pm\ \pi$ (the upper and lower symmetry planes are at $\theta = \pm\ \pi/4$).

In Refs. 3 and 6, $\bar{x}$ is translated but not magnified whereas $\bar{\theta}$ is magnified as above. Unequal scaling is of course <u>not</u> conformal so that orthogonality of the grid cannot be maintained at the boundaries. The resulting grid in the $x - \theta$ plane will be highly flattened and thus highly nonorthogonal.

On an $\bar{r}$ = constant surface the boundaries and coordinate system in the $\bar{x} - \bar{\theta}$ plane are sketched in Fig. 6. Because of symmetry, only the region $-\ \pi \leq \bar{\theta} \leq 0$ needs to be considered. The airfoil can be unwrapped by applying the conformal transformation,

$$\bar{x} + i\bar{\theta} = \ell n\left[1 - \cosh(\xi + i\eta)\right] \quad . \qquad (21)$$

Equation (21) maps the region below the $\bar{x}$-axis to positive ξ in the band $0 \leq \eta \leq \pi$. We note that the sign of $\bar{\theta}$ in Eq. (21) follows Caughey & Jameson [3] so that a right-handed coordinate system results. In Ref. 6, the sign of $\bar{\theta}$ was negative which produced a left-handed system. Figure 7 presents a schematic of the boundaries in the $\xi - \eta$ plane. The initial value line (IVL) A-B-C is seen to map into a near semi-circle.

Following Ref. 6, the corners at points A and C can be eliminated by applying the conformal transformation,

$$\bar{\xi} + i\bar{\eta} = \xi + i\eta + \frac{\xi_0^2}{\xi + i\eta} \quad , \tag{22}$$

where ξ_0 is defined in Fig. 7. Equation (22) has the effect of nearly straightening out the IVL. The geometry of the boundaries in the $\bar{\xi} - \bar{\eta}$ plane is shown in Fig. 8.

In Ref. 6 a shearing transformation is used to produce a grid in the $\bar{\xi} - \bar{\eta}$ plane. For airfoils with non-zero trailing edge angles this procedure produces discontinuous metric coefficients across the line $\bar{\xi} = \bar{\xi}_F$. To eliminate the effect of the corner at the trailing edge (point F) a procedure similar to the generation of the smooth curves in the meridian plane is used. The $\bar{\xi} - \bar{\eta}$ coordinates are first translated and rotated about point F according to

$$\left.\begin{aligned} \hat{x} &= (\bar{\xi}_F - \bar{\xi})\cos\lambda_{F_-} + (\bar{\eta}_F - \bar{\eta})\sin\lambda_{F_-} \\ \hat{y} &= -(\bar{\xi}_F - \bar{\xi})\sin\lambda_{F_-} + (\bar{\eta}_F - \bar{\eta})\cos\lambda_{F_-} \end{aligned}\right\} \quad , \tag{23}$$

where the positive $\hat{x}$ axis points toward point E, the airfoil leading edge, and λ_{F_-} is the trailing edge angle in the $\bar{\xi} - \bar{\eta}$ plane. The translated and rotated $\bar{\xi} - \bar{\eta}$ boundaries are sketched in Fig. 9.

The final step in producing a smooth boundary is to apply a hinge point transformation to $(\hat{x},\hat{y})$ to eliminate the corner at point F. Equation (1) applies provided $z = \hat{x} + i\hat{y}$ and

$$n = \frac{\pi}{\pi - \Delta\lambda} \quad , \tag{24}$$

where

$$\Delta\lambda = \lambda_{F_-} - \lambda_{F_+} \quad . \tag{25}$$

The resulting boundary in the hinge plane is sketched in Fig. 10. Once a grid in the hinge plane is produced by transfinite interpolation, the transformation sequence is reversed to obtain the grid in the $x - \theta$ plane.

The FORTRAN coding is written in terms of real variables which involves determining the real and imaginary parts of the conformal transformations as well as their inverses. These relations are given in the appendix.

Corner Point Projection on Airfoil

Part of the present grid generation strategy is to force one of the coordinate lines normal to the airfoil to pass through point C, the corner point. This point on the airfoil is denoted by letter K -- see Fig. 10. Such a line provides a natural division between those lines intersecting the airfoil from the IVL, B-C, and the lower symmetry line, C-J.

An effective method of locating point K that prevents reflexes on the connecting segment C-K is to construct a circular arc between C and K which is normal to both boundaries. Under this assumption the relation between the coordinates at C and K is found to be

$$\frac{u_C - u_K}{v_K - v_C} = \tan\left[\frac{1}{2}\left(\phi_C + \phi_K\right)\right] \quad , \tag{26}$$

where

$$\tan \phi = \frac{du}{dv} \quad . \tag{27}$$

Supplementing Eq. (26) by the equation for the airfoil image, $v_S(u)$, gives two equations for the two unknowns u_K and v_K.

Equation (26), together with the airfoil image equation, can be solved iteratively by the following formula, derivable from Newton's method:

$$u_K^{(n+1)} = u_K^{(n)} + \Delta u_K^{(n)} \tag{28}$$

where

$$\Delta u_K^{(n)} = \left\{ \frac{u_C - u_K + (v_C - v_K)\tan[\frac{1}{2}(\phi_C + \phi_K)]}{1 + \tan \phi_K \tan[\frac{1}{2}(\phi_C + \phi_K)]} \right\}^{(n)} \quad . \tag{29}$$

The right-hand-side of Eq. (29) is evaluated from values at point K at the n^{th} iteration level. In the determination of $v_K^{(n)}$ and $\tan \phi_K^{(n)}$, Lagrange cubic interpolation is used. Convergence of u_K is quite rapid, requiring usually about four or five iterations to reach $|\Delta u_K| < 10^{-6}$. Once $(u,v)_K$ are known, $(\bar{x},\bar{\theta})_K$ are found by the inverse transformation of the mapping sequence.

Stretching Functions

In the $x - \theta$ plane the two-sided stretching function of Vinokur is used to generate the grid point distributions on the stagnation streamline B-E and the airfoil-wake centerline E-K-F-I. For segment B-E a single stretching function is used whereas for segment E-K-F-I, a sequence of three stretching functions is required.

The two-sided stretching function for the normalized variable t is given by

$$t = \frac{\tanh(\xi\Delta\phi)}{A \sinh \Delta\phi + (1 - A \cosh \Delta\phi)\tanh(\xi\Delta\phi)} \quad , \tag{30}$$

where ξ is the normalized generating variable of constant step size, $\Delta\phi$ is the solution of the transcendental equation

$$B = \frac{\sinh \Delta\phi}{\Delta\phi} \tag{31}$$

and

$$A = (S_0/S_1)^{1/2} \tag{32}$$

$$B = (S_0 S_1)^{1/2} \tag{33}$$

and S_0 and S_1 are dimensionless slopes defined as

$$S_0 = \frac{d\xi}{dt}(0) \quad ,$$

$$S_1 = \frac{d\xi}{dt}(1) \quad ,$$

which control the clustering at t = 0 and t = 1.

The reason for using two-sided stretching functions on segments E-K, K-F and F-I is to provide clustering at all segment end points. It is needed at point E because of the rapid drop in pressure downstream of the stagnation point, at point K to provide a more nearly uniform grid distribution on the inflow line and at points F and I to resolve the flow at the airfoil trailing edge and tail of the body respectively. Since the arc length step size at points K and F should be continuous, not all of the parameters (S_0, S_1) are

independent. If (S_0, S_1) are specified on E-K and S_1 is specified on K-F, then S_0 on these latter segments must be calculated to satisfy continuity of step size at the segment junctions. The relation is

$$(S_0)_{KF} = (S_1)_{EK} \cdot \frac{s_{KF}}{s_{EK}} \cdot \frac{N_{EK}}{N_{KF}} \quad , \tag{34}$$

where s denotes arc length of the segment and N the number of intervals on the segment. A similar expression holds on segment F-I.

Transfinite Interpolation

Normalized pseudo-computational variables $\hat{\xi}$ and $\hat{\eta}$ are defined such that the interior of the quadrilateral in Fig. 10 in the u - v plane transforms to the interior of the unit square in the $\hat{\xi}$ - $\hat{\eta}$ plane. The transformation from the computational domain to the hinge-plane domain is given in terms of the position vector $\vec{r}$:

$$\vec{r}(\xi,\eta) = \begin{bmatrix} u(\hat{\xi},\hat{\eta}) \\ \\ v(\hat{\xi},\hat{\eta}) \end{bmatrix} \quad , \tag{35}$$

where $0 \leq \hat{\xi} \leq 1$, $0 \leq \hat{\eta} \leq 1$.

Specifying the distribution of the position vector $\vec{r}$ and its normal derivatives on the four boundaries in the $\hat{\xi}$ - $\hat{\eta}$ plane is equivalent to defining the grid on the boundaries in the hinge plane and ultimately, the x - θ plane.

The transfinite interpolation method used here is the extension of Eriksson [1] as specialized by Vinokur and Lombard [5]. The relation for $\vec{r}$, using point-of-compass notation for the boundaries, is

$$\begin{aligned}
\vec{r}(\hat{\xi},\hat{\eta}) = {} & \vec{r}_S(\hat{\xi})E(\hat{\eta}) + \vec{r}_N(\hat{\xi})F(\hat{\eta}) + \vec{r}_{\eta_S}(\hat{\xi})G(\hat{\eta}) + \vec{r}_{\eta_N}(\hat{\xi})H(\hat{\eta}) \\
& + E(\hat{\xi})[\vec{r}_W(\hat{\eta}) - \vec{r}_{SW}E(\hat{\eta}) - \vec{r}_{NW}F(\hat{\eta}) - \vec{r}_{\eta_{SW}}G(\hat{\eta}) - \vec{r}_{\eta_{NW}}H(\hat{\eta})] \\
& + F(\hat{\xi})[\vec{r}_E(\hat{\eta}) - \vec{r}_{SE}E(\hat{\eta}) - \vec{r}_{NE}F(\hat{\eta}) - \vec{r}_{\eta_{SE}}G(\hat{\eta}) - \vec{r}_{\eta_{NE}}H(\hat{\eta})] \\
& + G(\hat{\xi})[\vec{r}_{\xi_W}(\hat{\eta}) - \vec{r}_{\xi_{SW}}E(\hat{\eta}) - \vec{r}_{\xi_{NW}}F(\hat{\eta}) - \vec{r}_{\xi\eta_{SW}}G(\hat{\eta}) - \vec{r}_{\xi\eta_{NW}}H(\hat{\eta})] \\
& + H(\hat{\xi})[\vec{r}_{\xi_E}(\hat{\eta}) - \vec{r}_{\xi_{SE}}E(\hat{\eta}) - \vec{r}_{\xi_{NE}}F(\hat{\eta}) - \vec{r}_{\xi\eta_{SE}}G(\hat{\eta}) - \vec{r}_{\xi\eta_{NE}}H(\hat{\eta})]
\end{aligned} \tag{36}$$

where E, F, G and H are cubic blending functions given by

$$\left.\begin{aligned}
F(u) &= u^2(3 - 2u) \\
G(u) &= u(1 - u)^2 \\
H(u) &= u^2(u - 1) \\
E(u) &= 1 - F(u)
\end{aligned}\right\} . \tag{37}$$

Equation (36) thus provides a smooth blending on the interior of the given distribution of grid points and normal derivatives on the boundaries. A typical grid in the hinge plane obtained by transfinite interpolation is shown in Fig. 11.

The evaluation of the various derivatives on the boundaries in Eq. (36) follows the prescription given by Vinokur & Lombard and is presented in detail in Appendix II.

Addon Grid

The foregoing procedure produces a C-grid in the x - θ plane in the region upstream of the tail line I-J. Because $\hat{\xi}$ = constant lines in the upstream grid are normal to I-J (and I-J is straight as well as normal to the wake centerline), a downstream grid can easily be created which has continuity through first derivatives across I-J. The addon grid which has these characteristics is a Cartesian grid with the same θ distribution at I-J as the upstream grid. Distributing grid points on the x-direction downstream of I-J is accomplished by a one-sided Vinokur stretching function with the parameter S_0 determined by requiring continuity of Δx on either side of I-J.

2.4 Computational Grid

If indices i, j and k denote the coordinates $\hat{\xi}$, $\hat{\eta}$ and $\bar{r}$, then the computational coordinates x, y and z may be conveniently defined as

$$\left.\begin{aligned} X &= i - 1 \quad , \quad 1 \leq i \leq i_{max} \\ Y &= j - 1 \quad , \quad 1 \leq j \leq j_{max} \\ Z &= k - 1 \quad , \quad 1 \leq k \leq k_{max} \end{aligned}\right\} . \tag{38}$$

The advantage of this system is that the computational step size in the three directions is unity which simplifies the metric coefficient calculations.

3. Results and Discussion

The afterbody-fin grid generation code is called TAILGRID and consists of about 1600 FORTRAN statements. It is written in double precision arithmetric and computes in terms of real variables only. To date all grid generation has been done on a VAX 11/782 computer with CPU per grid point found to be about 7×10^{-3} sec. Thus computing a surface containing 1500 points requires approximately 10 sec.

The airfoil family chosen for testing the grid generation procedure was the NACA symmetric four digit series. The equation for this profile is

$$y_F = -5\tau\left(0.2969\sqrt{x} - 0.1281x - 0.3516x^2 + 0.2843x^3 - 0.1015x^4\right) , \qquad (39)$$

where τ is the maximum thickness expressed as a fraction of the chord. In the original equation for y_F, see Eq. (6.2) of Ref. 8, the coefficient of x is given as 0.12600 which causes the airfoil to have a finite trailing edge thickness $\left(y_{TE} = 0.0021\right)$. Since the grid generation procedure requires zero trailing edge thickness, the coefficient of x was modified as shown in Eq. (39). Interpolation is used liberally on the airfoil in the grid generation process; thus an accurate definition of y_F versus x is a necessity. Usually 100 points on the airfoil are computed for this purpose with clustering at the leading edge.

A number of 2-D test cases in the $x - \theta$ plane were run to determine the effect of certain input parameters on grid quality. These cases all consisted of an NACA 0012 airfoil at a cylindrical radius of 0.5. The common parameters for the five cases are given in Table 1 while the parameters that vary from case to case are presented in Table 2.

N1	N2	JMAX	DOB	SXO	SX2	SX3	SY1
10	20	31	1.0	5.0	2.0	1.1	1.0

Table 1. Common Parameters in 2-D Test Cases.

Case	DIVL	SX1	SYO
1	0.5	1.0	2.0
2	0.5	3.0	2.0
3	0.5	3.0	50.0
4	1.0	3.0	50.0
5	1.5	3.0	50.0

Table 2. Variable Parameters in 2-D Test Cases.

In all of the above cases, the point distributions on inflow-lower symmetry line and outflow boundaries are determined as described in the previous section. In this 2-D example only the grid point distribution downstream of the trailing edge is given by a geometric progression.

Case 1 and 2, shown in Figs. 12 and 13, are the same except that clustering is used about point K in case 2 and none is used in case 1. The orthogonality constraint is seen to produce considerable spreading of $\hat{\xi}$ = constant lines

near the corner (point C). Without clustering a poor boundary point distribution on the IVL is obtained whereas with clustering the distribution close to point C is improved.

Case 3, presented in Fig. 14, is similar to case 2 except that the clustering parameter on the stagnation line at the airfoil leading edge is 25 times larger. The result is a much more dense grid near the airfoil surface which would be useful for calculation of viscous flow at high Reynolds number. In both cases the number of points on the stagnation line is the same -- 31.

Cases 4 and 5 (see Figs. 15 and 16) show what happens to the grid when d_{IVL} is increased, all other parameters being the same as in case 3. Point K is seen to migrate toward the airfoil leading edge as d_{IVL} increases which results in a squeezing of grid lines between the leading edge and point K. In terms of grid quality the optimum value of d_{IVL} appears to lie between 0.5 and 1.0 so that line C-K remains nearly straight. One way of moving the IVL further upstream without sacrificing grid quality would be to add a cartesian grid upstream of the flattened C-grid with the same θ-spacing as on line B-C (the IVL for the C-grid).

For a 3-D test problem the afterbody meridian profile was represented by the following analytic function:

$$r_b(\mu) = r_{b_1} F(\mu) - d_{bod} \tan \hat{\theta}_T G(\mu) \quad , \tag{40}$$

where

$$\mu = - \frac{x}{d_{bod}} \quad ,$$

d_{bod} = afterbody length ,

r_{b_1} = initial afterbody radius ,

and F and G are the cubic blending functions defined by Eq. (37). The particular values chosen for the afterbody parameters are

$$r_{b_1} = 0.75 \quad , \quad d_{bod} = 2.5 \quad , \quad \tan \hat{\theta}_T = 0.50 \quad ,$$

which produce a fairly full profile with a tail half angle of 26.6 degrees. Other parameters in the test problem are given in Table 3.

N1	N2	N3	N4	JMAX	KMAX	DIVL	DTL	DOB
10	20	5	10	31	3	0.75	0.5	1.0
RTIP	TAU	SX0	SX1	SX2	SX3	SY0	SY1	SY0
1.0	0.2	5.0	3.0	2.0	2.0	2.0	1.0	2.0

Table 3. Parameters in 3-D Test Problem.

Only one intermediate surface was generated in the test problem to serve as an illustration of the general features of these surfaces.

The meridian plane view of the test problem geometry, computational domain and intermediate surface is shown in Fig. 17. Two views of each $\bar{r}$ = constant surface are presented, the first from below and in front and the second from the side. These views are shown in Figs. 18 through 23. A composite side view showing the position of each surface relative to the other is presented in Fig. 24.

In a grid stacking procedure each grid on a surface is generated somewhat independently of the other. The dependence is indirect through the geometry and not direct as in the case of partial differential equation grid generation schemes or fully 3-D algebraic schemes. Thus for 3-D grids generated by stacking one of the primary concerns is with smoothness in the stacking direction. In the present method, the only reason that the grid changes in the $x - \theta$ plane from surface to surface is that the airfoil image is changing. As $\bar{r}$ increases, the airfoil image, according to Eq. (17), is shrinking in terms of maximum thickness approximately as $1/r_s$. Although the total arc length of the airfoil image is also shrinking slightly as $\bar{r}$ increases, the clustering parameters are fixed and hence the airfoil point distribution on each surface is always in the same proportion. As the airfoil image grows thinner, point K slowly moves toward the leading edge. The trace of point K in the meridian plane is shown in Fig. 17. On the other hand, the distribution of points on the stagnation line remains the same independent of $\bar{r}$. Of course close to the surface of the afterbody in the vicinity of the tail the grid shrinks rapidly to reflect the pointed nature of the tail and the axis singularity. This feature would exist whether or

not stacking were used. Thus because the airfoil image is varying slowly as $\bar{r}$ increases and the points on the image remain in the same proportion of arc length, the present method can be expected to produce a grid of high quality in the stacking direction.

One aspect of the current strategy of point placement on boundaries is not entirely satisfactory. Although the circular arc method of point placement in the hinge plane works well on the lower symmetry line, it leaves something to be desired on the IVL. Coupled with the singularity at the corner (point C) and the orthogonality requirement at boundaries, clustering at point K was found to be necessary to achieve a reasonable point spacing near point C on the IVL. This clustering would probably not be necessary if a different strategy were used to locate the points on the IVL. One possibility would be to space them in the $x - \theta$ plane in the same proportion of arc length as along the airfoil between the leading edge and point K. Downstream of point K the strategy would remain as before.

REFERENCES

(1) Eriksson, L. E., "Generation of Boundary-Conforming Grids Around Wing-Body Configurations using Transfinite Interpolation," AIAA Jour., 20, 1313-1320 (1982).

(2) Smith, R. E., Jr. and R. A. Kudlinski, "Algebraic Grid Generation for Wing-Fuselage Bodies," AIAA Paper 84-0002, presented at AIAA 22nd Aerospace Sciences Meeting, Reno, NV (9-12 January 1984).

(3) Caughey, D. A. and A. Jameson, "Numerical Calculation of Transonic Potential Flow about Wing-Body Combinations," AIAA Jour., 17, 175-181 (1979).

(4) Shmilovich, A. and D. A. Caughey, "Grid Generation for Wing-Tail-Fuselage Configurations," in Advances in Grid Generation, ASME FED - Vol. 5, 189-197, presented at Applied Mechanics, Bioengineering, and Fluids Engineering Conference, Houston, TX (20-22 June 1983).

(5) Vinokur, M. and C. K. Lombard, "Algebraic Grid Generation with Corner Singularities," in Advances in Grid Generation, ASME FED - Vol. 5, 99-106, presented at Applied Mechanics, Bioengineering and Fluids Engineering Conference, Houston, TX (20-22 June 1983).

(6) Hoffman, G. H., "Grid Generation about a Fin-Cylinder Combination," ARL/PSU TM 83-45, Applied Research Laboratory, The Pennsylvania State University (30 March 1983).

(7) Vinokur, M., "On One-Dimensional Stretching Functions for Finite-Difference Calculations," NASA CR-3313 (October 1980).

(8) Abbott, Ira H. and A. E. Von Doenhoff, Theory of Wing Sections, Dover Publishers (1959).

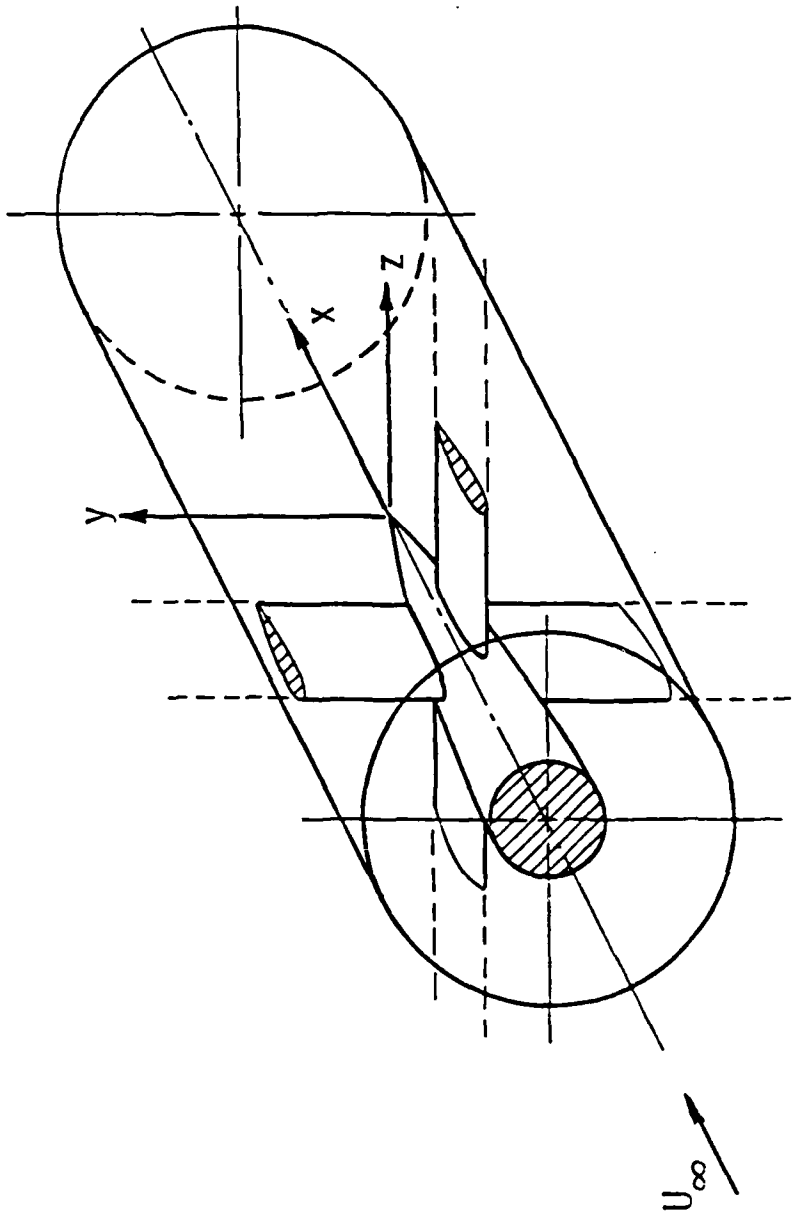

Figure 1. Schematic of Geometry and Computational Domain.

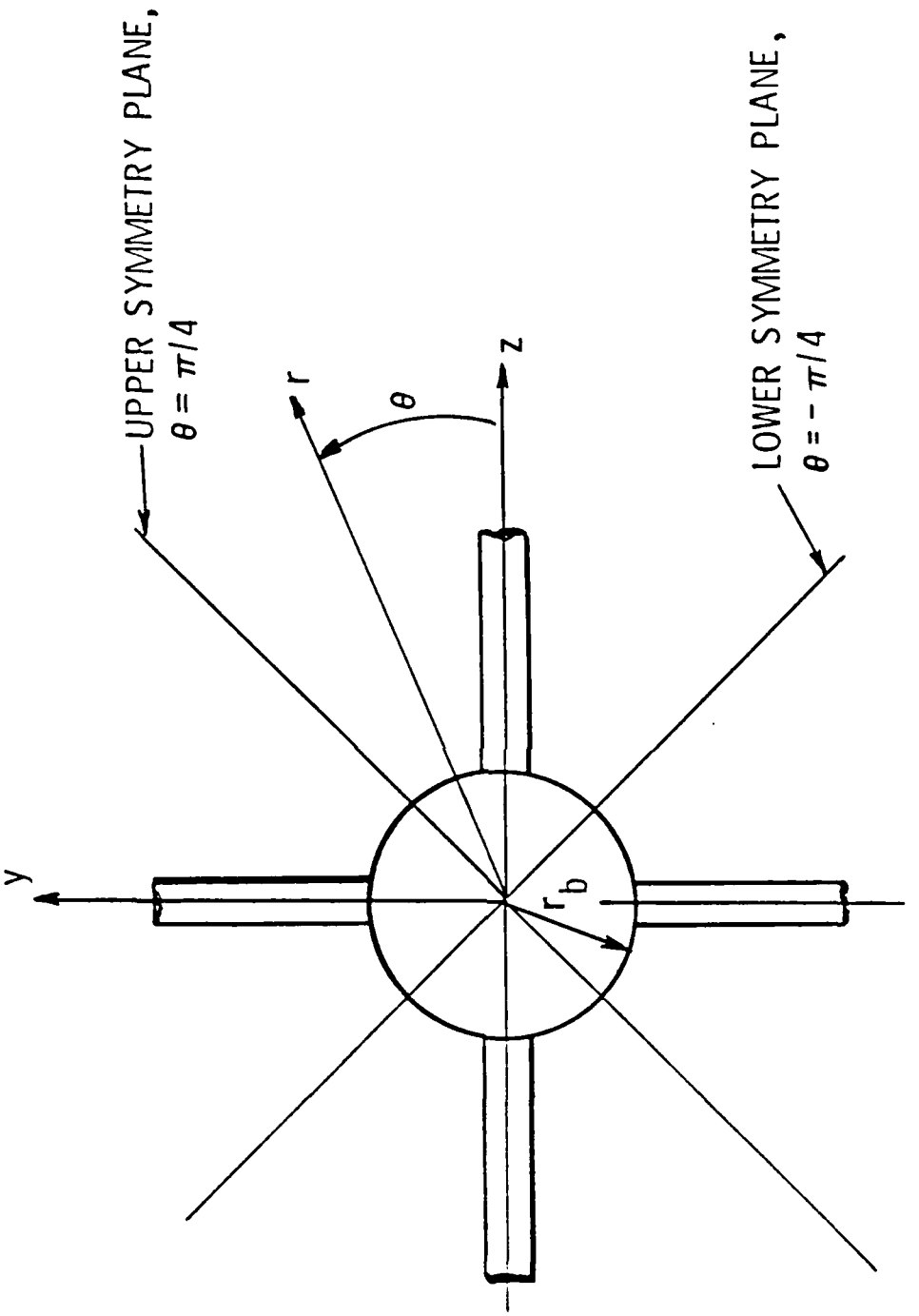

Figure 2. Planes of Symmetry.

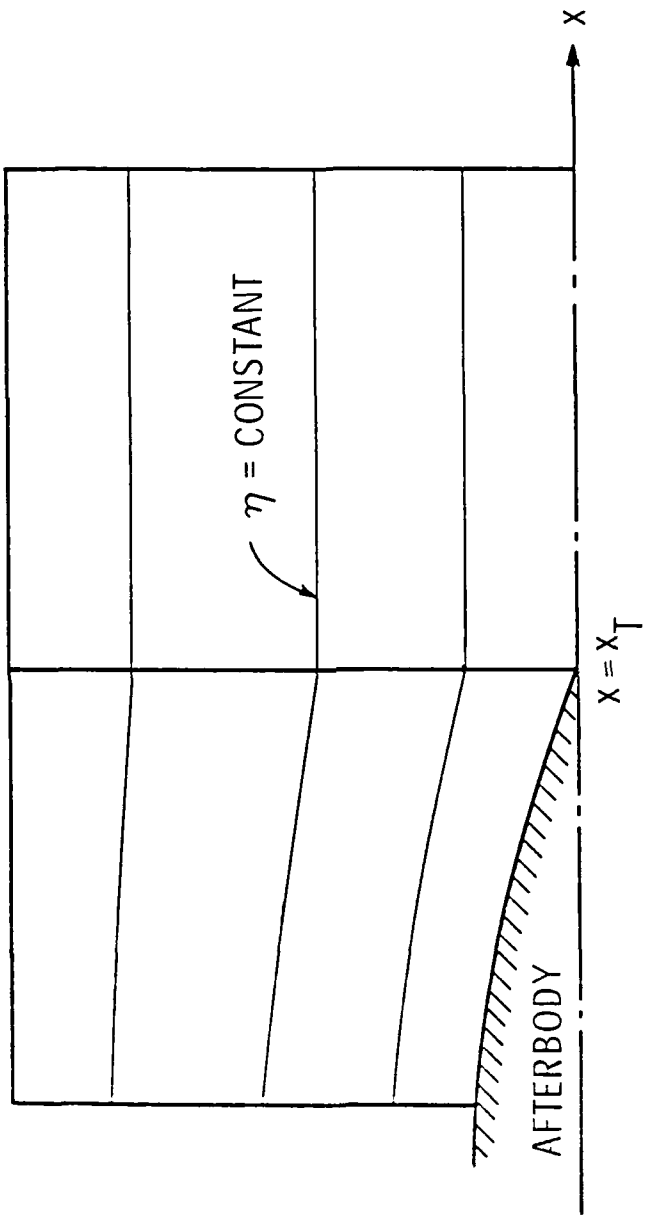

Figure 3. Grid in Meridian Plane using Shearing Transformation.

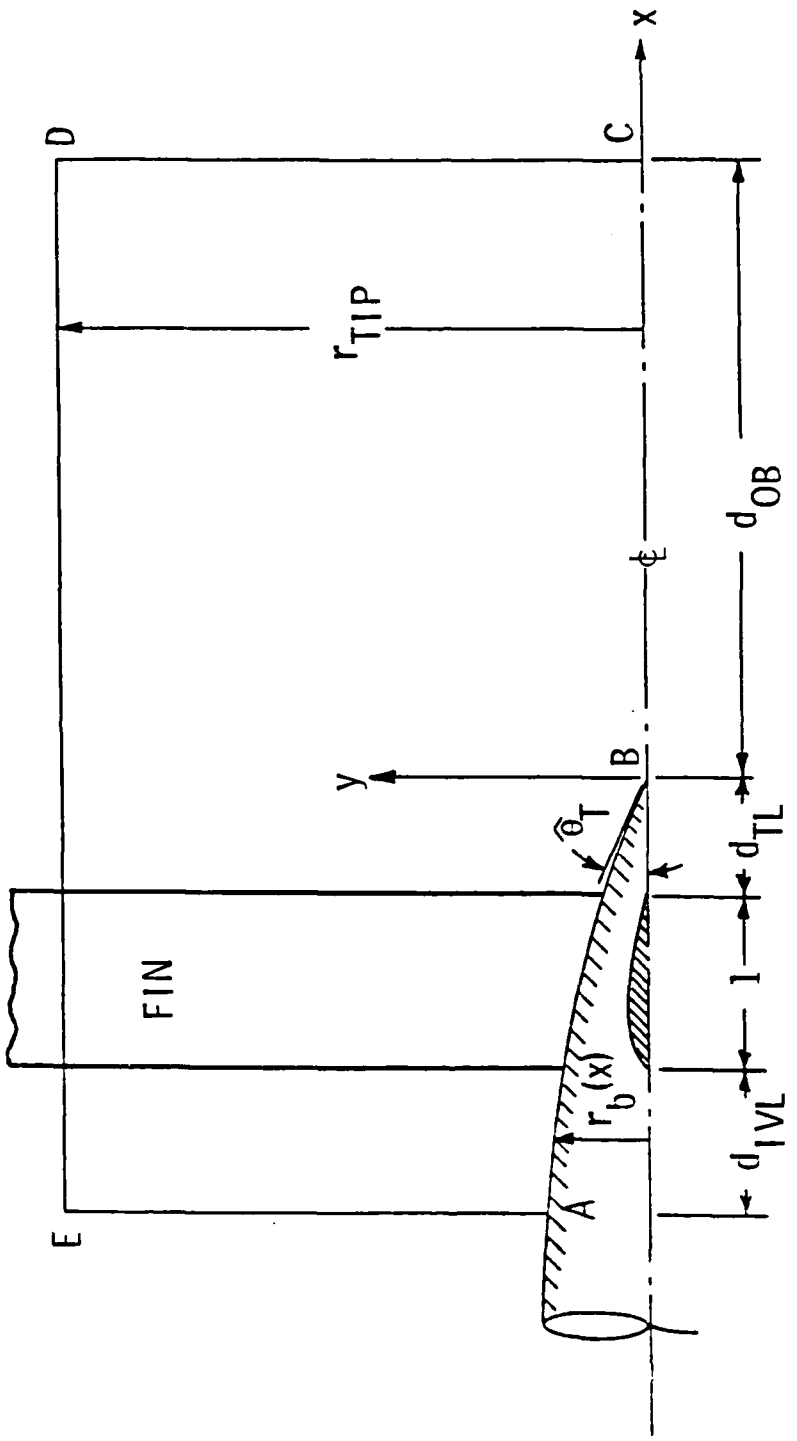

Figure 4. Meridian Plane View of Geometry and Computational Domain.

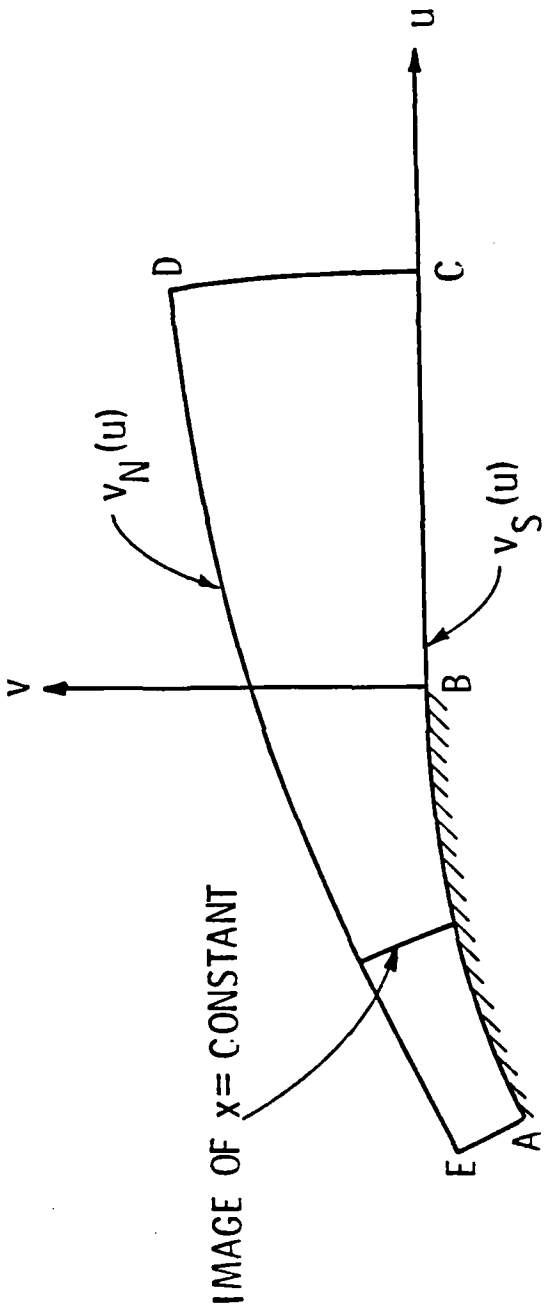

Figure 5. Meridian Boundary Image in Hinge Plane.

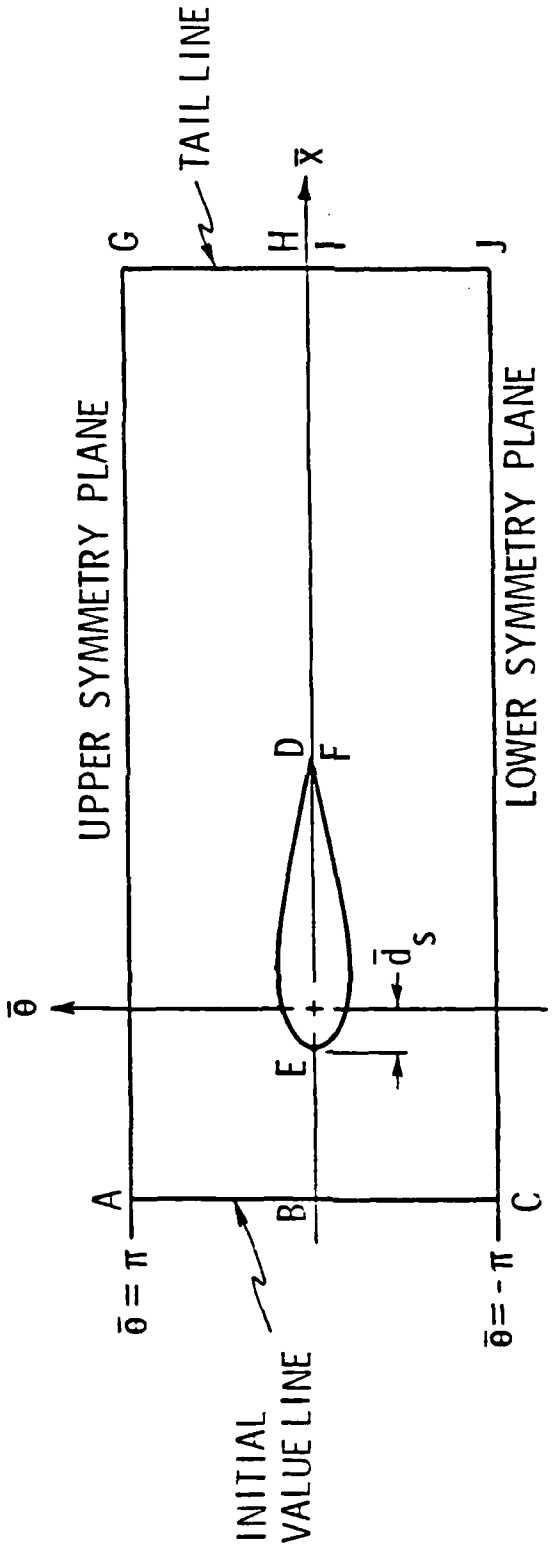

Figure 6. Computational Domain, $\bar{r}$ = Constant Surface.

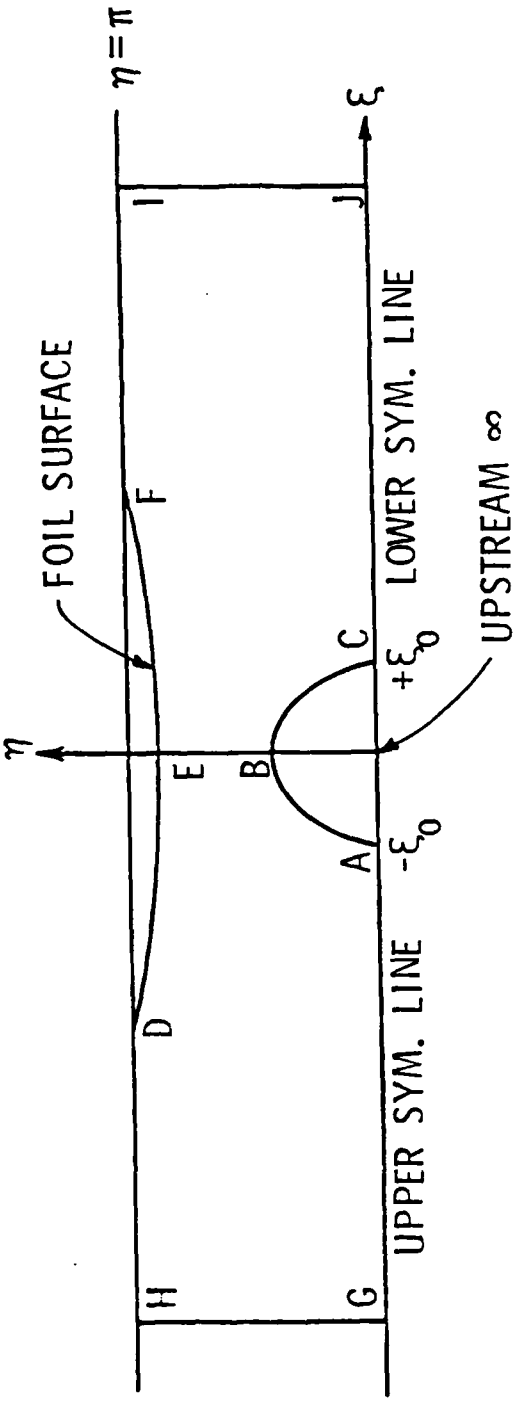

Figure 7. Boundaries in ξ - η Plane.

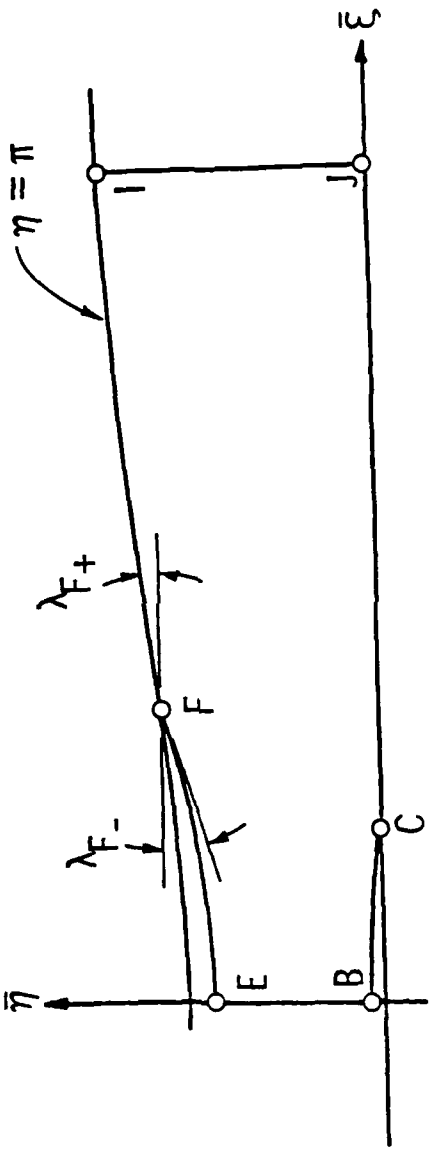

Figure 8. Boundaries in Positive $\bar{\xi} - \bar{\eta}$ Plane.

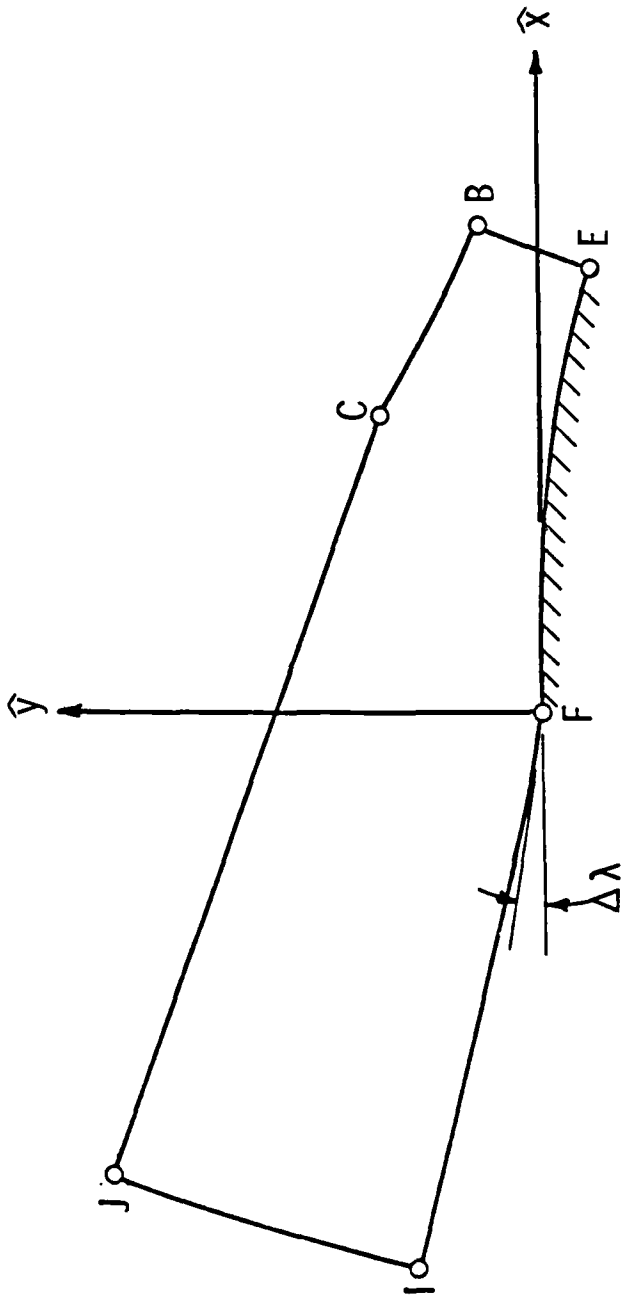

Figure 9. Translated and Rotated Boundaries in $\hat{x}$ - $\hat{y}$ Plane.

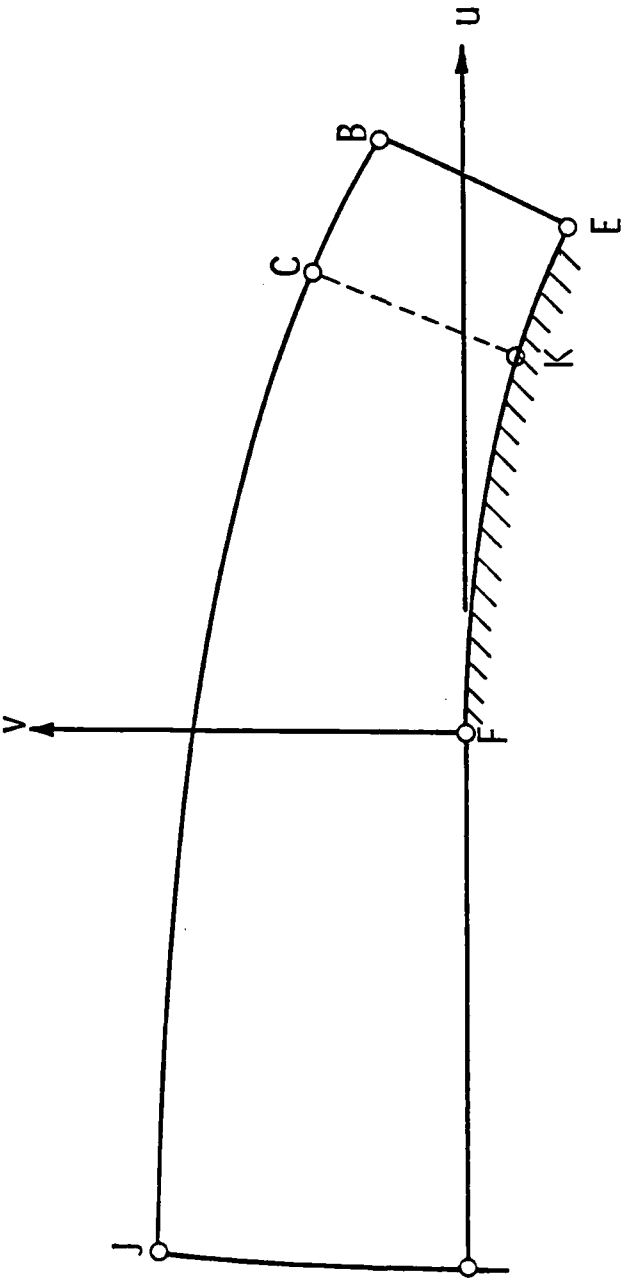

Figure 10. Boundaries in Hinge Plane.

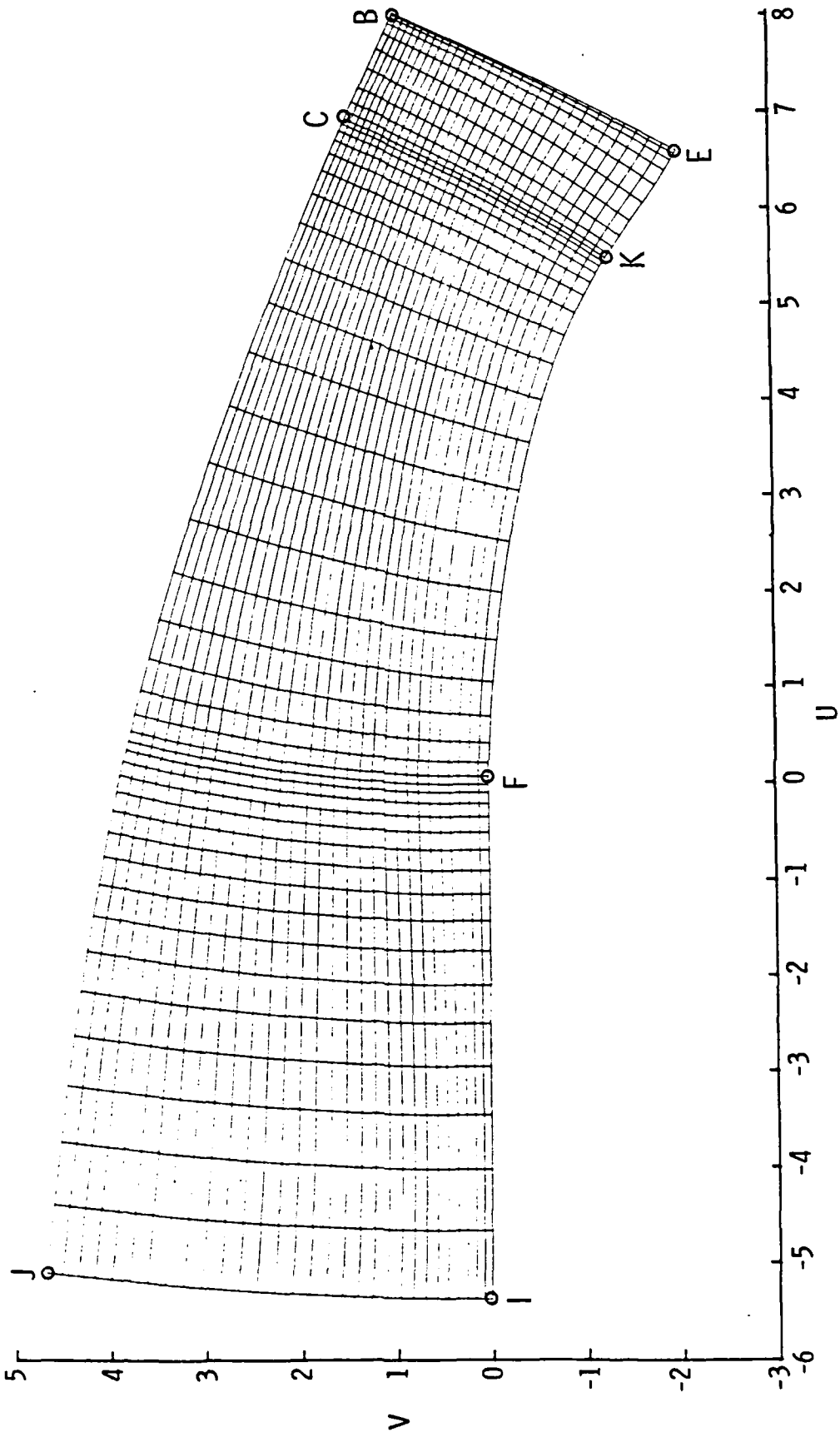

Figure 11. Typical Grid in Hinge Plane using Transfinite Interpolation.

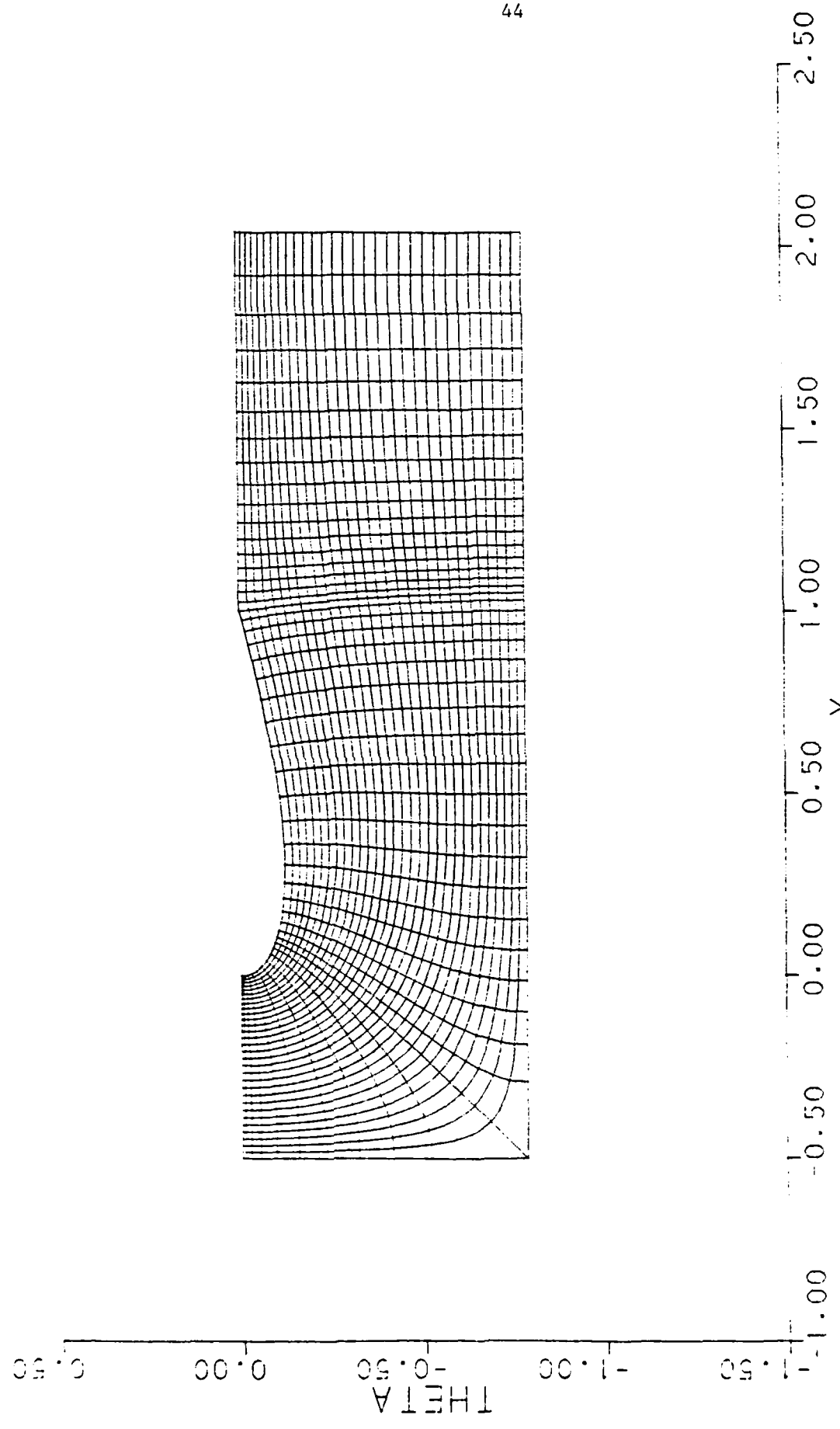

Figure 12. Case 1, No. Clustering at Point K.

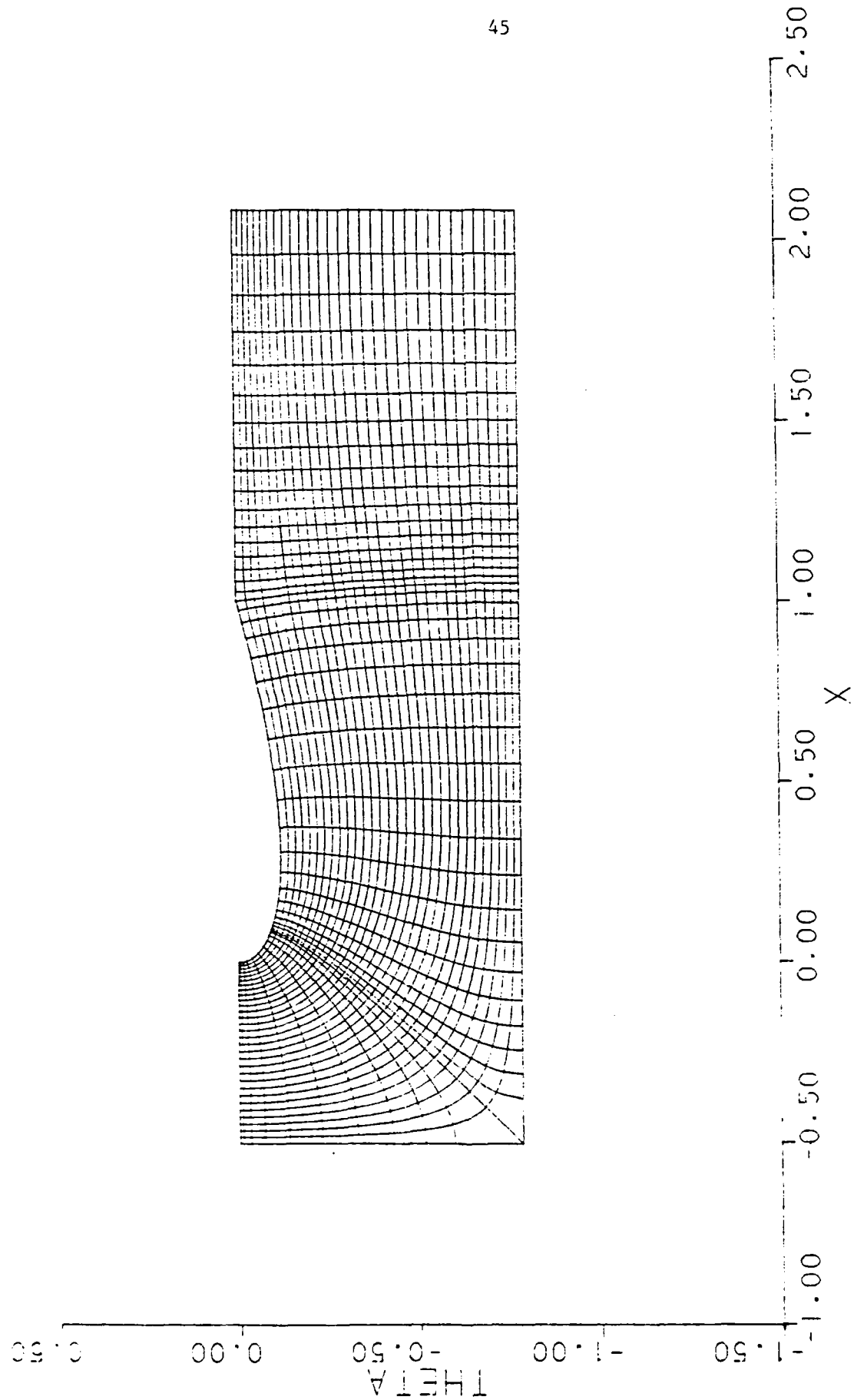

Figure 13. Case 2, Clustering at Point K.

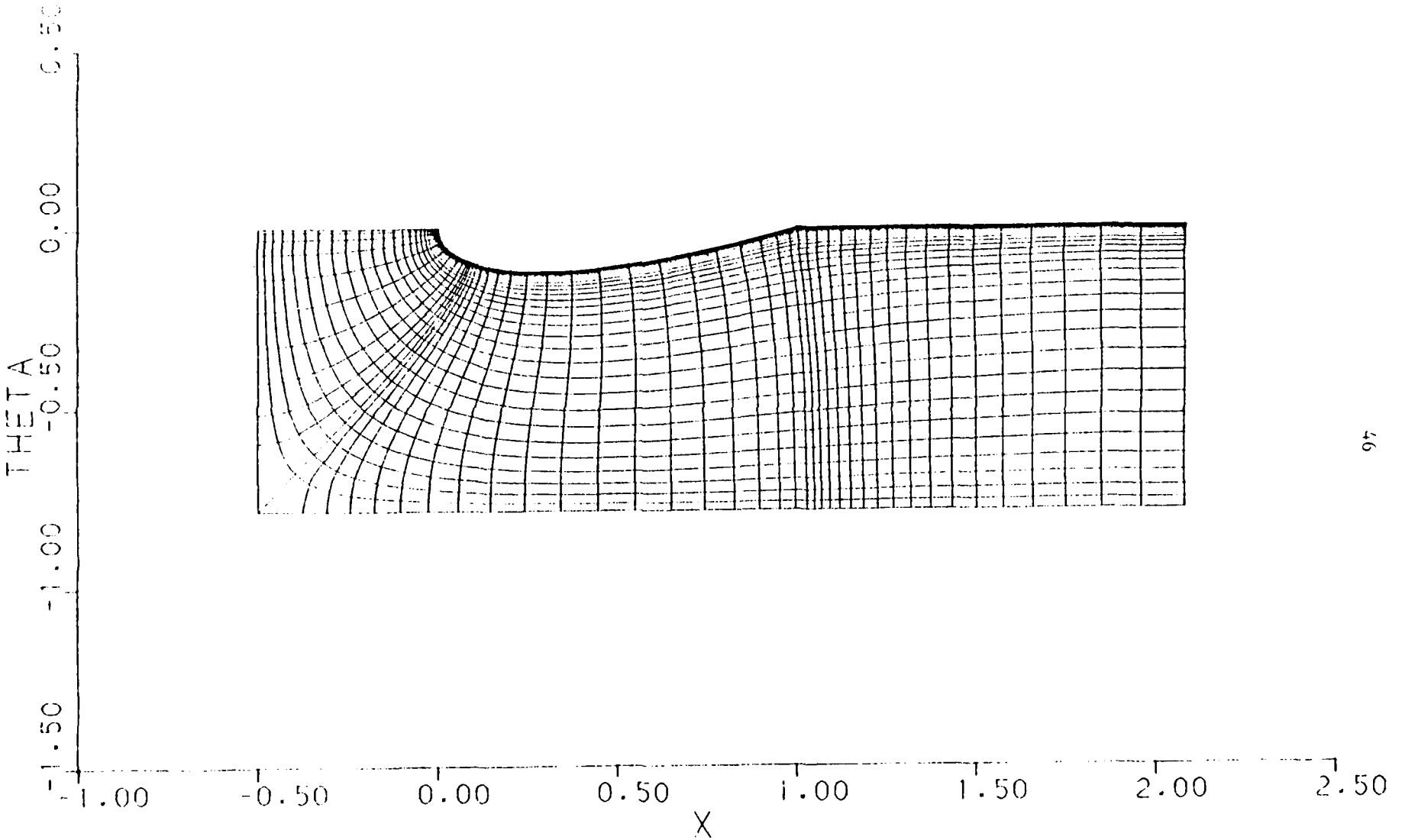

Figure 14. Case 3, Clustering at Airfoil Surface.

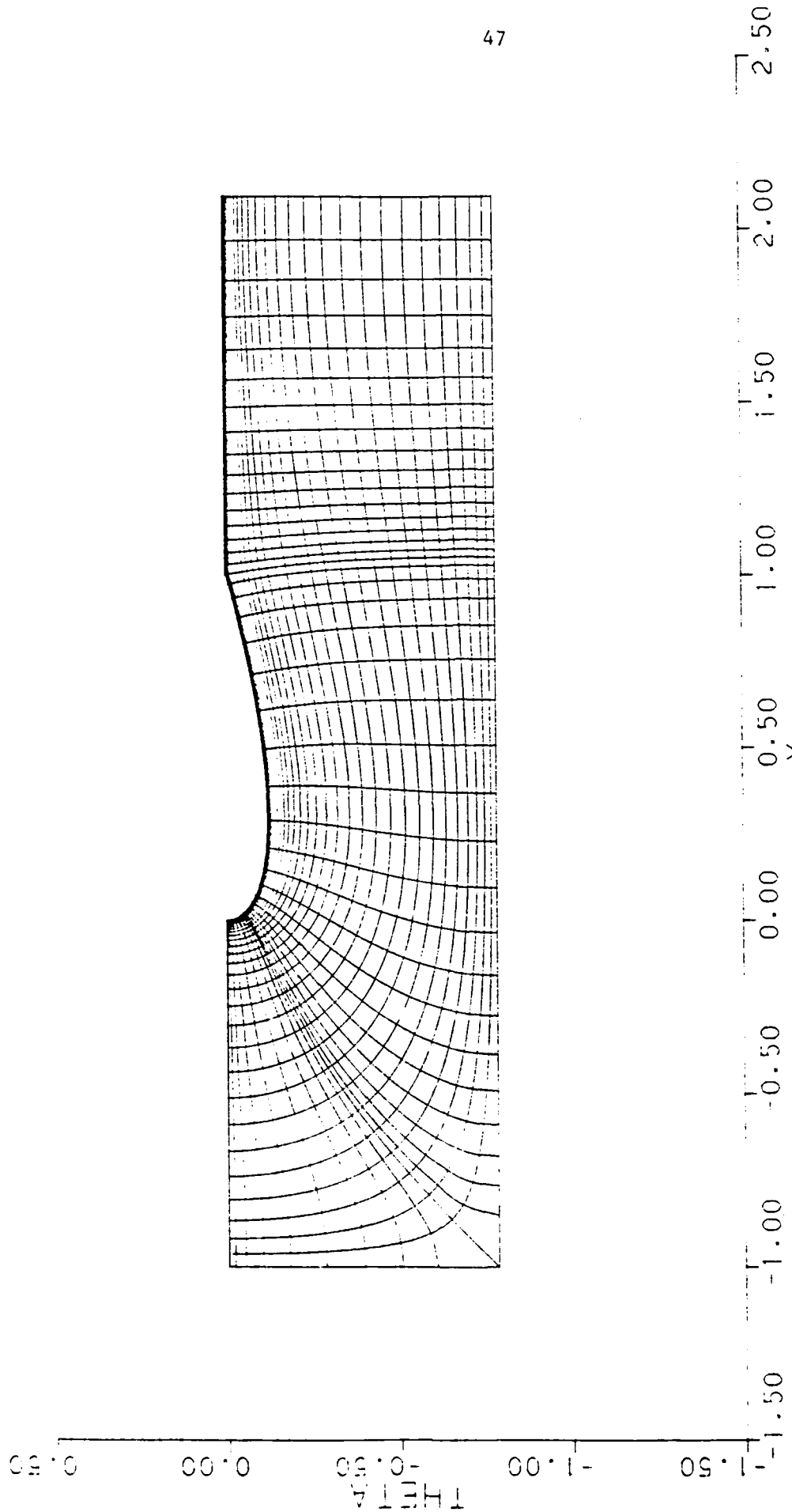

Figure 15. Case 4, Intermediate Upstream Position of Initial Value Line.

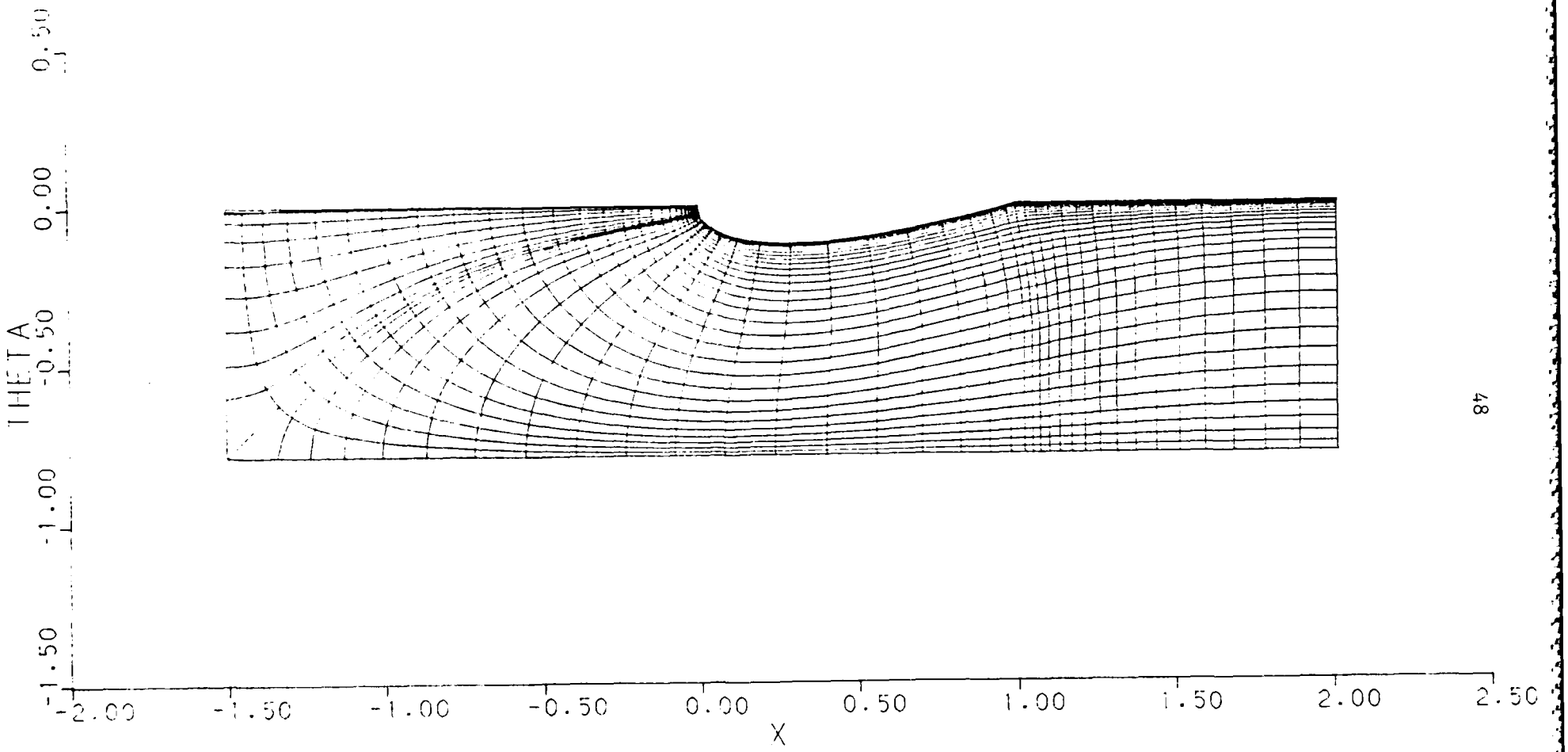

Figure 16. Case 5, Extreme Upstream Position of Initial Value Line.

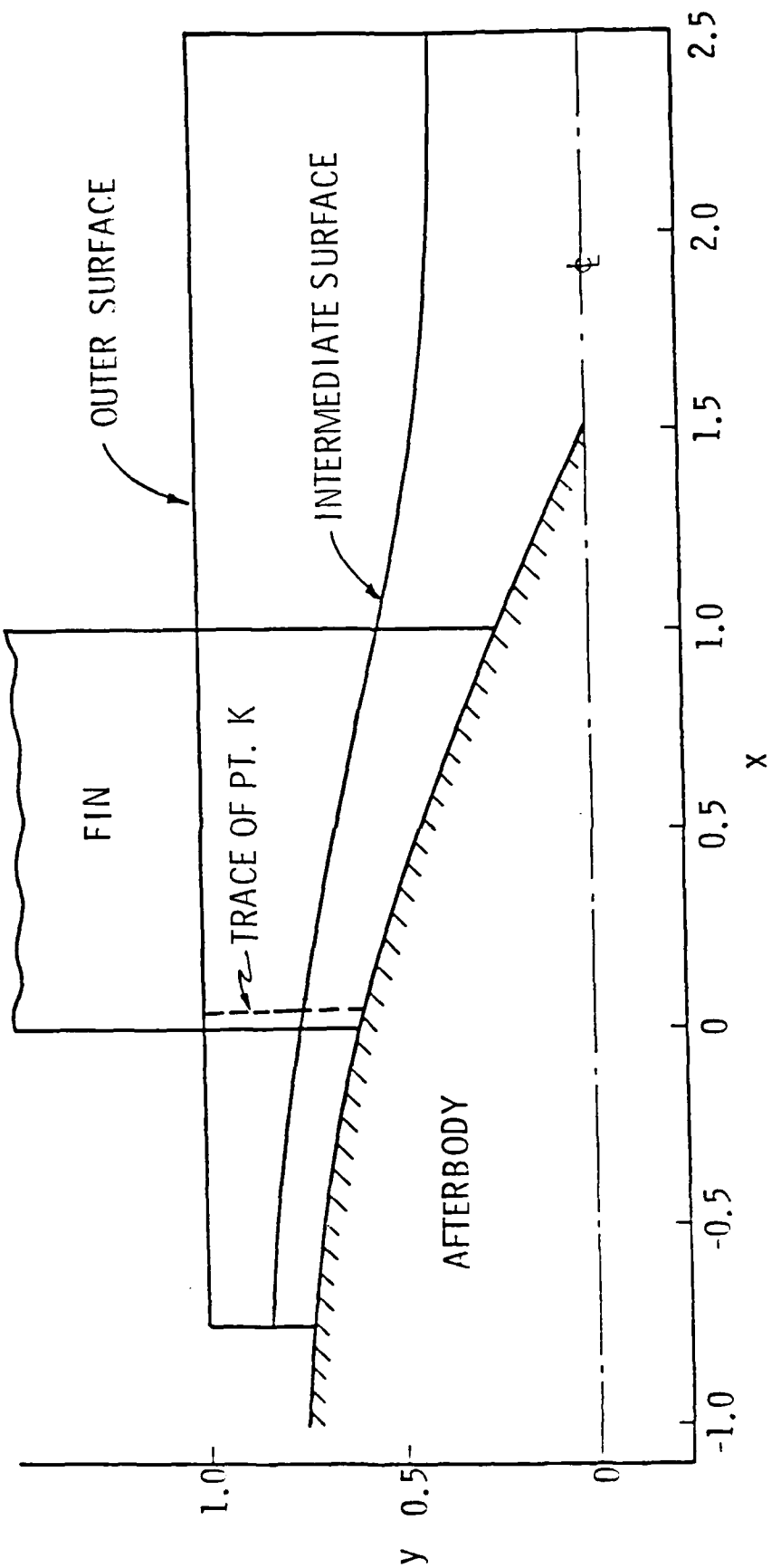

Figure 17. Meridian Plane View of Test Problem Geometry.

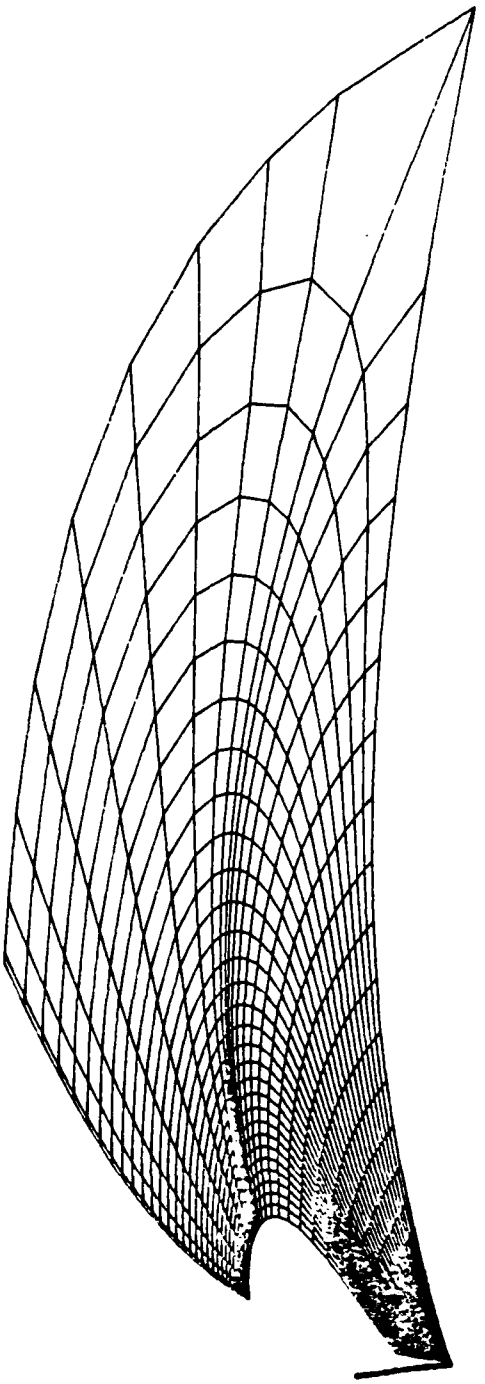

Figure 18. Front View of Afterbody Grid.

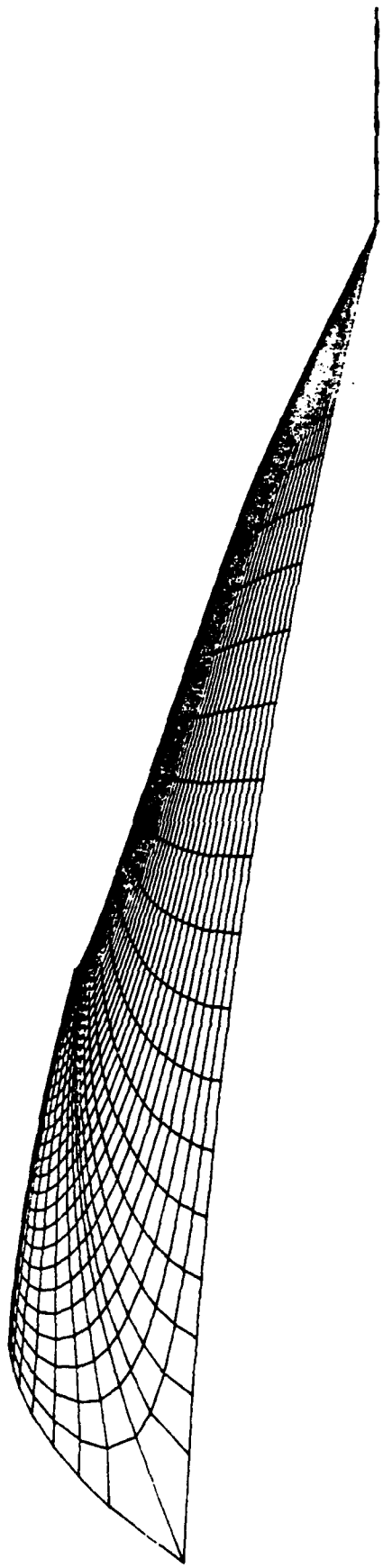

Figure 19. Side View of Afterbody Grid.

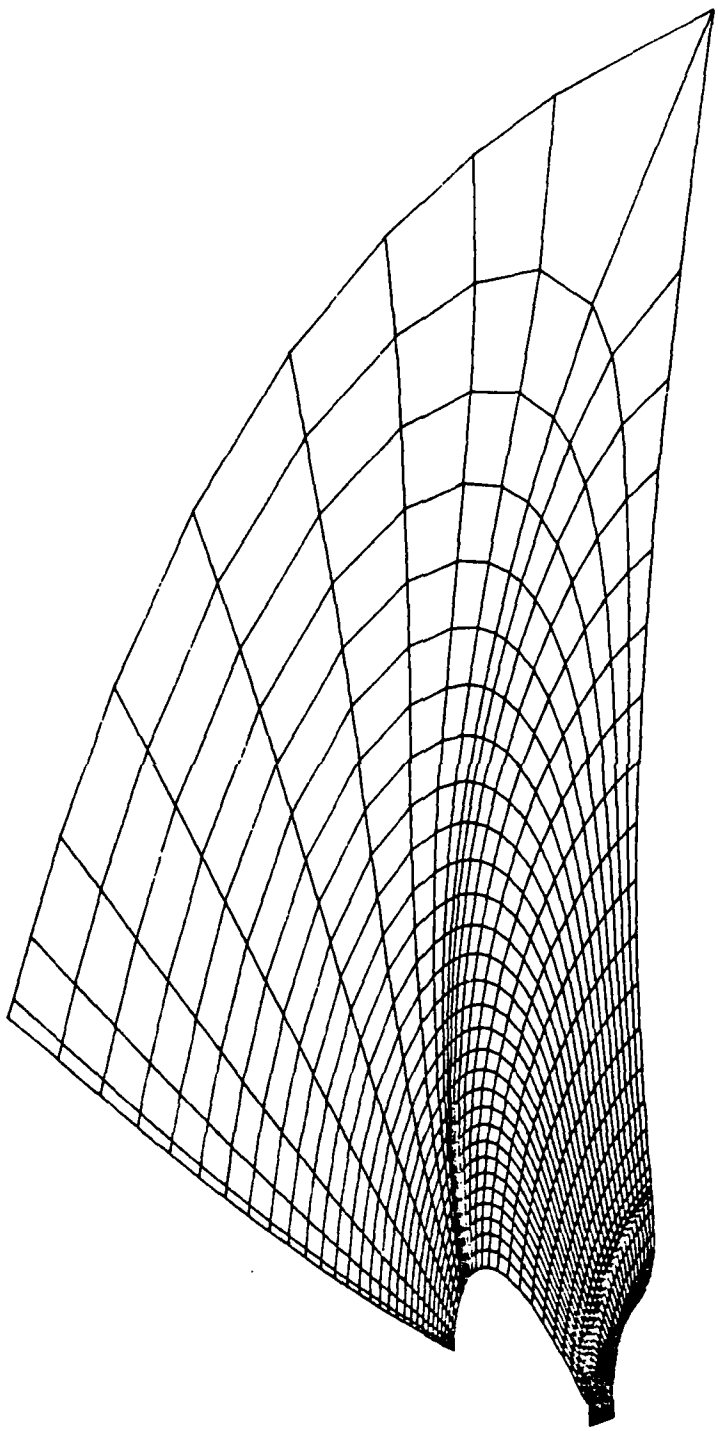

Figure 20. Front View of Intermediate Surface Grid.

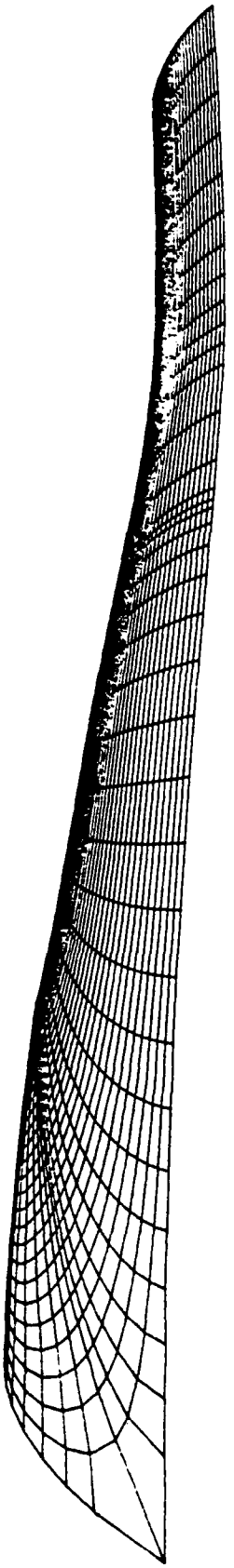

Figure 21. Side View of Intermediate Surface Grid.

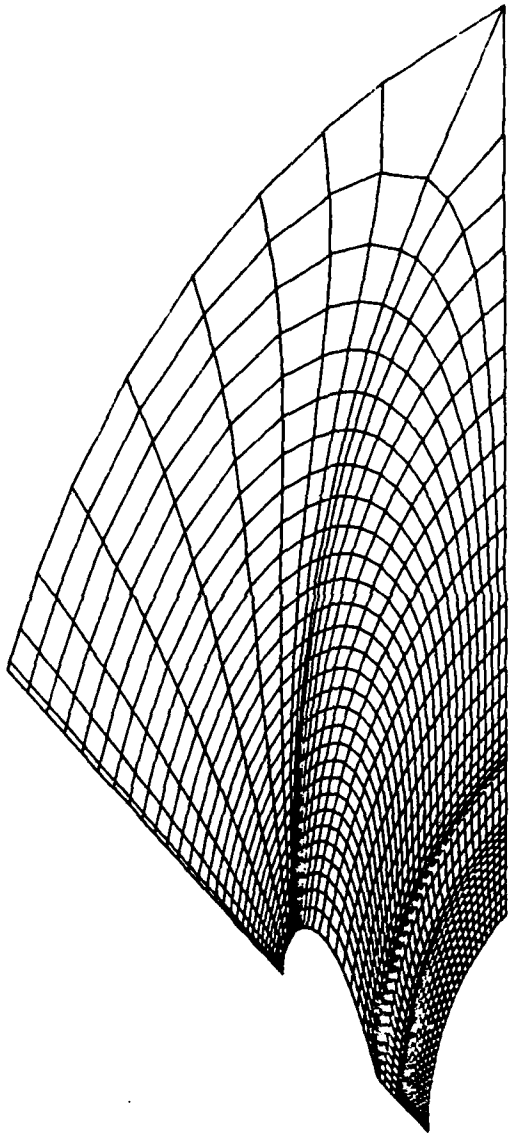

Figure 22. Front View of Outer Surface Grid.

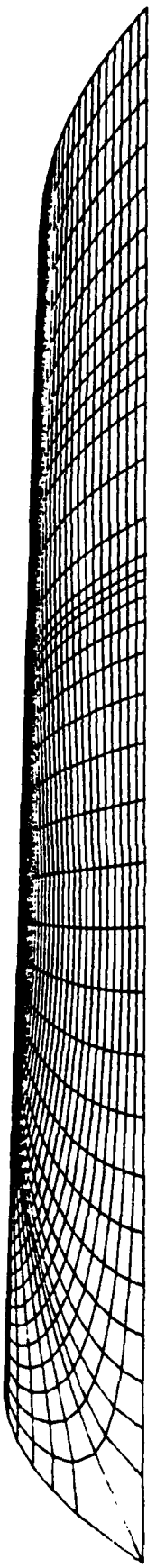

Figure 23. Side View of Outer Surface Grid.

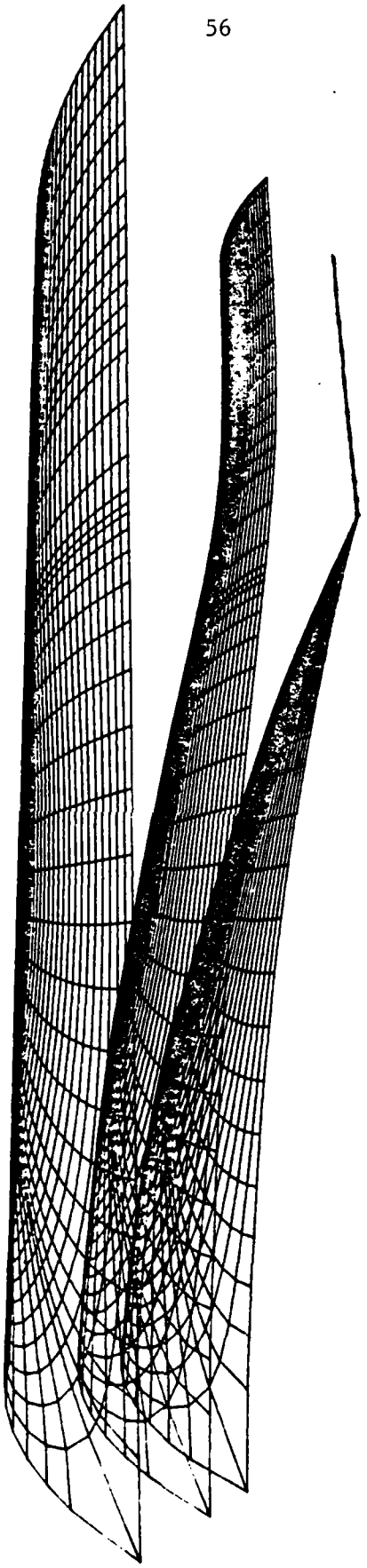

Figure 24. Composite View of Afterbody, Intermediate and Outer Surface Grids.

Appendix I. Conformal Mapping Relations

(1) Transformation from $\bar{x} - \bar{\theta}$ to $\bar{\xi} - \bar{\eta}$ plane.

$$\xi = \sinh^{-1}\{\tfrac{1}{2}\left[\beta + \left(\beta^2 + 4\bar{q}^{-2}\right)^{1/2}\right]\}^{1/2} , \qquad \text{(AI.1)}$$

$$\eta = \cos^{-1}\left(-\frac{\bar{p}}{\cosh \xi}\right) , \qquad \text{(AI.2)}$$

where

$$\beta = \bar{p}^{-2} + \bar{q}^{-2} - 1 , \qquad \text{(AI.3)}$$

$$\bar{p} = e^{\bar{x}} \cos \bar{\theta} - 1 , \qquad \text{(AI.4)}$$

$$\bar{q} = e^{\bar{x}} \sin \bar{\theta} , \qquad \text{(AI.5)}$$

and

$$\bar{\xi} = \xi\left(1 + \bar{\mu}\right) , \qquad \text{(AI.6)}$$

$$\bar{\eta} = \eta\left(1 - \bar{\mu}\right) , \qquad \text{(AI.7)}$$

where

$$\bar{\mu} = \frac{\xi_0^2}{\xi^2 + \eta^2} . \qquad \text{(AI.8)}$$

(2) Transformation from $\bar{\xi} - \bar{\eta}$ to $\bar{x} - \bar{\theta}$ plane.

$$\xi = \frac{1}{2}\,\bar{\xi} + \left[\frac{1}{2}\,(\mu + p)\right]^{1/2} \tag{AI.9}$$

$$\eta = \frac{1}{2}\,\bar{\eta} + \left[\frac{1}{2}\,(\mu - p)\right]^{1/2} \tag{AI.10}$$

where

$$\mu = \left(p^2 + 4q^2\right)^{1/2} \quad , \tag{AI.11}$$

$$p = \frac{1}{4}\left(\bar{\xi}^2 - \bar{\eta}^2\right) - \xi_0^2 \quad , \tag{AI.12}$$

$$q = \frac{1}{4}\,\bar{\xi}\bar{\eta} \quad , \tag{AI.13}$$

and

$$\bar{x} = \ell n(\cosh\,\xi - \cos\,\eta) \quad , \tag{AI.14}$$

$$\bar{\theta} = -\cos^{-1}\left(\frac{1 - \cosh\,\xi\,\cos\,\eta}{\cosh\,\xi - \cos\,\eta}\right) \quad . \tag{AI.15}$$

In the preceding relations ξ_0 is computed from

$$\xi_0 = \sinh^{-1}\left[\frac{4\,\exp(-a)}{1 - \exp(-a)}\right] \tag{AI.16}$$

where

$$a = 4\left(d_S + d_{IVL}\right) \quad . \tag{AI.17}$$

In the determination of d_s, the same procedure is followed here as in Ref. 6 where near the airfoil leading edge in the x - θ plane the most nearly orthogonal grid is sought. Such a system is obtained when the leading edge maps into an η = constant line. The resulting expression for d_s is found to be

$$d_s = \frac{1}{4} \ell n\left(\frac{1 + 4\rho_0}{1 + 2\rho_0}\right) \quad , \tag{AI.18}$$

where ρ_0 is the radius of curvature of the airfoil leading edge in the x - θ plane. Equation (AI.18) differs from its counterpart in Ref. 6, Eq. (100), because a uniform stretching of $\bar{x}$ and $\bar{\theta}$ is used here.

Appendix II. Evaluation of Boundary Derivatives for Transfinite Interpolation

Normalized coordinates $\hat{\xi}$ and $\hat{\eta}$ are determined in the hinge plane in terms of the normalized arc length along the south and east boundaries (lines E-K-F-I and B-E in Fig. 10). If s_1 and s_2 denote running arc length along the south and east boundaries, then

$$\hat{\xi}_i = \frac{(s_1)_i}{s_{E-I}} \quad , \tag{AII.1}$$

$$\hat{\eta}_i = \frac{(s_2)_j}{s_{B-E}} \quad , \tag{AII.2}$$

where the running arc lengths are determined using the chord approximation.

If $\vec{t}_1$ and $\vec{t}_2$ are unit tangent vectors along the $\hat{\xi}$ and $\hat{\eta}$ coordinate curves, then

$$\vec{r}_\xi = \frac{\partial s_1}{\partial \hat{\xi}} \vec{t}_1 \quad , \tag{AII.3}$$

and

$$\vec{r}_\eta = \frac{\partial s_2}{\partial \hat{\eta}} \vec{t}_2 \quad . \tag{AII.4}$$

Under the assumption that extended orthogonality holds at the corners the cross-derivative is given by

$$\vec{r}_{\hat{\xi}\hat{\eta}} = \frac{\partial s_1}{\partial \hat{\xi}} \frac{\partial s_2}{\partial \hat{\eta}} \left(C_2 \vec{t}_2 - C_1 \vec{t}_1 \right) \quad , \tag{AII.5}$$

where C_1 and C_2 are the curvatures of the $\hat{\xi}$ and $\hat{\eta}$ coordinate curves respectively.

The south-north and west-east boundaries are assumed always to be oriented as shown in Fig. 10. Thus on the south boundary we take $v_S = v_S(u)$ from which the unit tangent vector follows as

$$\vec{t}_1 = t_{1u}\vec{e}_u + \vec{t}_{1v}\vec{e}_v \quad , \tag{AII.6}$$

where

$$t_{1u} = \frac{1}{\left(1 + v_S'^2\right)^{1/2}} \quad , \tag{AII.7}$$

$$t_{1v} = \frac{v_S'}{\left(1 + v_S'^2\right)^{1/2}} \quad . \tag{AII.8}$$

and $\vec{e}_u$ and $\vec{e}_v$ are unit vectors in the u and v directions respectively. Then the unit normal vector to the south boundary may be written as

$$\vec{t}_2 = - t_{1v}\vec{e}_u + t_{2u}\vec{e}_v \quad . \tag{AII.9}$$

And finally, the curvature on the south boundary is

$$C_1 = \frac{v_S''}{\left(1 + v_S'^2\right)^{3/2}} \quad . \tag{AII.10}$$

On the east boundary we take $u_E = u_E(v)$ and hence the unit tangent vector is

$$\vec{t}_2 = t_{2u}\vec{e}_u + t_{2v}\vec{e}_v \quad , \tag{AII.11}$$

where

$$t_{2u} = \frac{u_E'}{\left(1 + u_E'^2\right)^{1/2}} \quad , \tag{AII.12}$$

$$t_{2v} = \frac{1}{\left(1 + u_E'^2\right)^{1/2}} \quad . \tag{AII.13}$$

Then the unit normal vector is

$$\vec{t}_1 = t_{2v}\vec{e}_u - t_{2u}\vec{e}_v \quad , \tag{AII.14}$$

and the curvature C_2 is

$$C_2 = - \frac{u_E''}{\left(1 + u_E'^2\right)^{3/2}} \quad . \tag{AII.15}$$

On the south boundary, from Eq. (AII.1)

$$\left(\frac{\partial s_1}{\partial \hat{\xi}}\right)_S = s_{E-I} \quad . \tag{AII.16}$$

The derivative $\partial s_2/\partial \hat{\eta}$ on the south boundary is known only at the end points and hence must be determined between points E and I by interpolation. Following Ref. 5, we use a cubic blending function approximation, viz.

$$\left(\frac{\partial s_2}{\partial \hat{n}}\right)_S = \left(\frac{\partial s_2}{\partial \hat{n}}\right)_{SW} E(\hat{\xi}) + \left(\frac{\partial s_2}{\partial \hat{n}}\right)_{SE} F(\hat{\xi}) + \left(\frac{\partial^2 s_2}{\partial \hat{\xi}\partial \hat{n}}\right)_{SW} G(\hat{\xi}) + \left(\frac{\partial^2 s_2}{\partial \hat{\xi}\partial \hat{n}}\right)_{SE} H(\hat{\xi}) \quad . \tag{AII.17}$$

From the extended orthogonality relations, the cross-derivative is found to be

$$\frac{\partial}{\partial \hat{\xi}}\left(\frac{\partial s_2}{\partial \hat{n}}\right) = \frac{\partial s_1}{\partial \hat{\xi}} \frac{\partial s_2}{\partial \hat{n}} C_2 \quad . \tag{AII.18}$$

On the east boundary, from Eq. (AII.2)

$$\left(\frac{\partial s_2}{\partial \hat{n}}\right)_E = s_{B-E} \quad , \tag{AII.19}$$

and analogous to Eq. (AII.17), the cubic blending function formula for $\partial s_1/\partial \hat{\xi}$ is

$$\left(\frac{\partial s_1}{\partial \hat{\xi}}\right)_E = \left(\frac{\partial s_1}{\partial \hat{\xi}}\right)_{SE} E(\hat{n}) + \left(\frac{\partial s_1}{\partial \hat{\xi}}\right)_{NE} F(\hat{n}) + \left(\frac{\partial^2 s_1}{\partial \hat{n}\partial \hat{\xi}}\right)_{SE} G(\hat{n}) + \left(\frac{\partial^2 s_1}{\partial \hat{n}\partial \hat{\xi}}\right)_{NE} H(\hat{n}) \quad . \tag{AII.20}$$

where from extended orthogonality

$$\frac{\partial}{\partial \hat{n}}\left(\frac{\partial s_1}{\partial \hat{\xi}}\right) = - \frac{\partial s_1}{\partial \hat{\xi}} \frac{\partial s_2}{\partial \hat{n}} C_2 \quad . \tag{AII.21}$$

To maintain a reasonable spacing of $\hat{\xi}$ = constant grid lines in the physical plane, especially near the airfoil surface, the normal spacing in the $x - \vartheta$ plane on the stagnation and outflow lines (east and west boundaries in the hinge plane) is taken to be the same. As a result $(n_j)_W$ does not obey a relation similar to Eq. (AII.2) and hence $\partial s_2/\partial \hat{n}$ must be

determined numerically point-by-point. As for $\partial s_1/\partial\hat{\xi}$, an interpolation relation similar to Eq. (AII.20) is used with appropriate changes in notation.

On the north boundary the points are positioned in the hinge plane by using a circular arc approximation similar to that used in locating point K. The iteration formula for u_N, similar to Eqs. (28) and (29) is

$$(u_N)_i^{(n+1)} = (u_N)_i^{(n)} + (\Delta u_N)_i^{(n)} \quad , \tag{AII.22}$$

where

$$(\Delta u_N)_i = \left\{ \frac{u_S - u_N + (v_S - v_N)\tan[\frac{1}{2}(\phi_S + \phi_N)]}{1 + \tan\phi_N \tan[\frac{1}{2}(\phi_S + \phi_N)]} \right\}^{(n)} \quad . \tag{AII.23}$$

The derivative $\partial s_1/\partial\hat{\xi}$ must be determined numerically at each point and $\partial s_2/\partial\hat{\eta}$ is computed from an interpolation formula analogous to Eq. (AII.17).

In the determination of the various interpolated values of u and v and their derivatives required in the foregoing equations, Lagrange cubic interpolation is used. The derivative expressions are determined by differentiation of the Lagrange polynomials.

DISTRIBUTION LIST FOR UNCLASSIFIED TECHNICAL MEMORANDUM 85-57,
by G. H. Hoffman, dated 12 April 1985

Defense Technical Information
Center
5010 Duke Street
Cameron Station
Alexandria, VA 22314
(Copies 1 through 6)

Commander
Naval Sea Systems Command
Department of the Navy
Washington, DC 20362
Attention: T. E. Peirce
Code NSEA-63R31
(Copy No. 7)

Commander
Naval Sea Systems Command
Department of the Navy
Washington, DC 20362
Attention: W. C. Sandberg
Code NSEA-55W33
(Copies 8 and 9)

Commander
Naval Sea Systems Command
Department of the Navy
Washington, DC 20362
Attention: J. J. Sejd
Code NSEA-05R24
(Copy No. 10)

Office of Naval Research
800 North Quincy Street
Department of the Navy
Arlington, VA 22217
Attention: C. Lee
Code 432
(Copy No. 11)

Office of Naval Research
800 North Quincy Street
Department of the Navy
Arlington, VA 22217
Attention: R. E. Whitehead
Code 432F
(Copy No. 12)

Commander
David W. Taylor Naval Ship
Research & Development Ctr
Department of the Navy
Bethesda, MD 20084
Attention: R. M. Coleman
Code 1843
(Copy No. 13)

Commander
David W. Taylor Naval Ship
Research & Development Ctr.
Department of the Navy
Bethesda, MD 20084
Attention: T. T. Huang
Code 1552
(Copy No. 14)

Commander
David W. Taylor Naval Ship
Research & Development Ctr.
Department of the Navy
Bethesda, MD 20084
Attention: Library
(Copy No. 15)

Commander
Naval Surface Weapons Center
Detachment
White Oak Laboratory
10901 New Hampshire Avenue
Silver Spring, MD 20903-5000
Attention: Library
(Copy No. 16)

Naval Research Laboratory
Department of the Navy
Washington, DC 20390
Attention: Library
(Copy No. 17)

Superintendent
Naval Post Graduate School
Monterey, CA 93949
Attention: Code 1424
(Copy No. 18)

NASA Lewis Research Center
21000 Brookpark Road
Cleveland, OH 44135
Attention: P. M. Sockol
Code MS 77-5
(Copy No. 19)

Dr. James E. Carter
Manager, Computational Fluid
Mechanics Research
United Technologies Research
Center
East Hartford, CT 06108
(Copy No. 20)

DISTRIBUTION LIST FOR UNCLASSIFIED TECHNICAL MEMORANDUM 85-57,
by G. H. Hoffman, dated 12 April 1985

Dr. R. E. Melnick
Director, Fluid Mechanics
Research & Development Ctr.
Grumman Aerospace Corporation
Bethpage, NY 11714
(Copy No. 21)

Dr. C. L. Merkle
Department of Mechanical Engineering
Mechanical Engineering Building
The Pennsylvania State University
University Park, PA 16802
(Copy No. 22)

Dr. Stanley Rubin
Department of Aerospace Engineering
and Applied Mechanics
The University of Cincinnati
Cincinnati, OH 45221
(Copy No. 23)

Dr. Frank A. Thames
Theoretical Aerodynamics Branch
Transonic Aerodynamics Division
Mail Stop 259
NASA Langley Research Center
Hampton, VA 23665
(Copy No. 24)

Dr. Joe F. Thompson
Department of Aerospace Engineering
Drawer A
Mississippi State University
Mississippi State, MS 39762
(Copy No. 25)

Director
Applied Research Laboratory
The Pennsylvania State University
Post Office Box 30
State College, PA 16804
Attention: S. A. Abdallah
(Copy No. 26)

Director
Applied Research Laboratory
The Pennsylvania State University
Post Office Box 30
State College, PA 16804
Attention: R. E. Henderson
(Copy No. 27)

Director
Applied Research Laboratory
The Pennsylvania State University
Post Office Box 30
State College, PA 16804
Attention: G. H. Hoffman
(Copy No. 28)

Director
Applied Research Laboratory
The Pennsylvania State University
Post Office Box 30
State College, PA 16804
Attention: K. C. Kaufman
(Copy No. 29)

Director
Applied Research Laboratory
The Pennsylvania State University
Post Office Box 30
State College, PA 16804
Attention: B. R. Parkin
(Copy No. 30)

Director
Applied Research Laboratory
The Pennsylvania State University
Post Office Box 30
State College, PA 16804
Attention: GTWT Files
(Copy No. 31)

Director
Applied Research Laboratory
The Pennsylvania State University
Post Office Box 30
State College, PA 16804
Attention: ARL/PSU Library
(Copy No. 32)

END

FILMED

7-85

DTIC